The global climate response to High-Latitude Low-Altitude Stratospheric Aerosol Injection (HiLLA-SAI)

Alistair Duffey[1, 2], Walker Lee[3], Lauren Wheeler[4], Peter Irvine[5], Benjamin Wagman[6], Matthew Henry[7], Daniele Visioni[8], Michel Tsamados[1], and Douglas MacMartin[9]

[1]Department of Earth Sciences, University College London, London, UK
[2]Reflective, San Francisco, USA
[3]Climate & Global Dynamics Division, National Science Foundation's National Center for Atmospheric Research, Boulder, CO, USA
[4]Atmospheric Sciences Department, Sandia National Laboratories, Albuquerque, NM, USA
[5]Department of Geophysical Sciences, University of Chicago, Chicago, Illinois, 60637, United States
[6]Earth Systems Analysis Department, Sandia National Laboratories, Albuquerque, NM, USA
[7]Department of Mathematics, University of Exeter, Exeter, UK
[8]Department of Earth and Atmospheric Sciences, Cornell University, Ithaca, NY, USA
[9]Sibley School of Mechanical and Aerospace Engineering, Cornell University, Ithaca, NY, USA

Correspondence: Alistair Duffey (alistair.duffey.21@ucl.ac.uk)

Abstract. High-latitude low-altitude (HiLLA) Stratospheric Aerosol Injections (SAI) would face fewer logistical barriers than high-altitude low-latitude SAI, because it could use repurposed existing large aircraft for deployment. However, relative to high-altitude SAI, it is expected to have reduced global cooling efficiency, and the more polar forcing profile and reduced tropical stratospheric heating would result in many differences in the surface climate response. Here, we present the first multi-model simulations of HiLLA-SAI, in UKESM1, CESM2-WACCM and E3SMv3. Using these simulations, we assess the global climate response to HiLLA-SAI, and the sensitivity to the latitude, altitude (13 km versus 15 km), seasonality and longitude of injections. For seasonal injections at 60°N/S and 13 km, all models show similar global cooling efficiency, of around 0.6°C per 12 Mt SO_2 per year, 40-53% of the equivalent cooling efficiency for 21 km injection in the tropics. Raising the injection height to 15 km increases this global cooling efficiency by around half, to 63-70% of the high altitude tropical case. The effects of HiLLA-SAI are more polar focused than other SAI strategies, particularly for the 13 km injection case, and large changes in sea-ice in both hemispheres, high-latitude precipitation and the polar seasonal cycle are shown. Nevertheless, our results highlight that HiLLA-SAI would still be a global intervention. For 13 km injection, tropical temperature change per unit global temperature change is 61-75% of the equivalent ratio under greenhouse-gas forced warming, and is larger in the 15 km case. Precipitation changes and sulfur deposition are also found at all latitudes. Overall, our results highlight the importance of further study into HiLLA-SAI strategies, which these simulations suggest could be a viable early-stage SAI deployment strategy, with global, not just polar, impacts.

1 Introduction

Stratospheric aerosol injection (SAI) is a proposed means of reducing global temperature rise and associated changes in climate by adding aerosols or their precursors to the stratosphere (Crutzen, 2006; NASEM, 2021; UNEP, 2023). These aerosols would scatter a small fraction of incoming sunlight, as occurs after some volcanic eruptions (Robock, 2000, 2013), producing a negative radiative forcing. Most scenarios of SAI envision deployment at altitudes greater than 20 km (Richter et al., 2022; Tilmes et al., 2018), well above the altitude at which existing large aircraft could deploy sufficient quantities of SO_2 (Smith et al., 2024). However, the tropopause is lower in the polar regions, making it plausible that deployment in the mid- to high-latitudes using existing commercial aircraft at altitudes near their limit (i.e. 13 - 15 km) could be a viable climate intervention (Duffey et al., 2025a). Such low-altitude deployment has been suggested as a potential strategy for the early years of a future deployment scenario (Wheeler et al., 2025). The reduced barriers to acquiring a fleet capable of this deployment strategy could also imply an increase in the number of actors able to participate in SAI and an earlier possible start date (Smith et al., 2024; Smith, 2024).

High-latitude SAI deployment has also been proposed as a means of reducing the rapid climate change ongoing in the Arctic (Robock et al., 2008; Lee et al., 2023a), which is warming three to four times faster than the global average (Rantanen et al., 2022) and is on track to be sea-ice free in summer by mid-century (Notz and Stroeve, 2018; Notz and Community, 2020; Bonan et al., 2021). Preventing or slowing the passing of cryospheric tipping points (e.g. Armstrong McKay et al., 2022), has also been proposed as a target of polar SAI deployments (Smith et al., 2024; Futerman et al., 2025), and in the Antarctic, SAI has been shown to reduce the loss of land ice (Goddard et al., 2023).

Motivated by these implications, several recent studies have assessed such 'high-latitude low-altitude' (HiLLA) scenarios in earth system models (Lee et al., 2021, 2023a; Wheeler et al., 2025; Duffey et al., 2025a). Here, we build on these studies to present the first multi-model comparison of simulations of HiLLA-SAI, using three earth system models – the UK Earth System Model (UKESM1), the Community Earth System Model (CESM2-WACCM), and the Energy Exascale Earth System Model (E3SMv3) – to investigate the global and polar climate impacts of HiLLA-SAI and their sensitivity to the altitude, latitude, longitude and seasonality of injection.

Deploying SAI in polar or sub-polar latitudes, and at lower altitudes, is expected to reduce the global cooling efficiency, defined as the magnitude of near-surface air temperature change per unit injected SO_2, for two main reasons. First, the combination of reduced distance in the stratosphere through which the aerosols sediment and a less favourable (i.e. more downwelling) background circulation decreases the aerosol lifetime and consequently the steady-state burden under a given injection rate (Niemeier et al., 2011; Tilmes et al., 2017; Lee et al., 2023b). In UKESM1, HiLLA-SAI strategies show lifetimes of 2-3 months, as compared to over 8 months for injection at 30°N/S and 20km (Duffey et al., 2025a). Qualitatively similar lifetimes are found by Lee et al. (2023a) for 15 km injection at 60°N in CESM2-WACCM, and in the earlier study of Robock et al. (2008), who simulate injection at 68°N at 10-15 km altitude. Given the short lifetime and the strong seasonality of insolation at high-latitudes, HiLLA strategies would necessarily be seasonal, with injection only during local spring/summer (Lee et al., 2021). Second, higher latitude injection would produce a more polar distribution of aerosols, such that they occur over regions

of lower insolation (except in local mid-summer) (North et al., 1981), high cloud cover (Intrieri et al., 2002), and high surface albedo, which all contribute to a reduced forcing per unit aerosol optical depth (e.g. Duffey et al., 2025a).

On the other hand, there are compensating effects which would oppose the decrease in efficiency for HiLLA strategies. As with the Arctic amplification of greenhouse-gas forced warming (e.g. Serreze and Francis, 2006; Taylor et al., 2022), local feedbacks – particularly the albedo, Planck and lapse rate (Pithan and Mauritsen, 2014) – also drive greater change in Arctic temperature for a given radiative forcing under SAI. This leads to greater absolute cooling in the Arctic than elsewhere under even low latitude injection in both UKESM1 (Henry et al., 2024) and CESM2-WACCM (Zhang et al., 2024). As a result, global mean temperature change is more susceptible to a given fractional restoration of Arctic than tropical climate (if counted over the same surface area of the planet). Additionally, aerosols with longer lifetimes are also larger on average, having more time to grow, and so can be less optically efficient (Kleinschmitt et al., 2018), although this effect is likely outweighed by the extra burden from increased lifetime (Lee et al., 2023b).

Beyond the reduced global cooling efficiency, HiLLA-SAI would result in many other important differences relative to the lower latitude and higher altitude SAI strategies which have been more commonly investigated. Drivers of these differences include the more polar and seasonal pattern of radiative forcing, and the strongly reduced tropical stratospheric heating (Bednarz et al., 2023a). Additionally, we expect a smaller tropical lower stratospheric water vapour increase due to a more polar aerosol burden under HiLLA-SAI, and greater lower-stratospheric ozone depletion due to the higher sulfate aerosol concentrations in the high latitudes (Bednarz et al., 2023a). In the context of volcanic eruptions, the natural analogue for SAI, low and high latitude eruptions are associated with different surface climate responses (Robock, 2000; Schneider et al., 2009; Sjolte et al., 2021). A strengthened polar vortex and positive North Atlantic Oscillation signal is associated with tropical stratospheric heating caused by low-latitude eruptions (Robock and Mao, 1992; Stenchikov et al., 2002; Zambri and Robock, 2016), but this effect is reduced (Schneider et al., 2009) or reversed (Sjolte et al., 2021) under high-latitude eruptions.

In this study, our simulations use an idealized injection strategy, injecting a constant mass of SO_2 each year at a single location in each hemisphere into the sub-polar lower stratosphere. This strategy is not designed to represent a plausible policy scenario. Instead, here, as with several previous intermodel comparisons of SAI (e.g. Kravitz et al., 2013; Visioni et al., 2023), we use a simple scenario to explore model sensitivities and inform future simulations of more complex HiLLA scenarios which could vary injections to target particular climate outcomes. We assess, first, the temperature change under HiLLA-SAI in the three models, globally and regionally. Second, we assess the aerosol distributions and optical depth (AOD), and the variation of these with the precise injection strategy. Third, we make a more detailed assessment of the response in the polar regions, including the seasonality of Arctic cooling and the sea-ice impacts. Finally, we briefly investigate several impacts which might be expected to differ between HiLLA and conventional high-altitude SAI: sulfate deposition, stratospheric ozone, and changes in tropical precipitation. Resolving the various uncertainties associated with the processes described here, to allow a comprehensive statement of the trade-offs between HiLLA and other SAI strategies, will require substantial further research. The results we describe have informed the design of a new GeoMIP experiment, G6-1.5K-HiLLA (Visioni et al., 2025), which will support this community research effort.

2 Methods

2.1 Earth System Models

We use an ensemble of simulations in three earth system models; UKESM1, CESM2-WACCM and E3SMv3. The version of UKESM1 used here – UKESM1.0 (Sellar et al., 2019) – has been used extensively to model SAI in recent years (Jones, 2019; Jones et al., 2021; Henry et al., 2023; Visioni et al., 2023; Bednarz et al., 2023b). The model uses HadGEM3-GC3.1 as the physical core (Kuhlbrodt et al., 2018), coupled to various earth system components including terrestrial and ocean biochemistry and dynamic vegetation (Sellar et al., 2019). There is a unified tropospheric and stratospheric chemistry model, UKCA (Archibald et al., 2020). The aerosol model, GLOMAP (Mann et al., 2010) is used with five log-normal modes (Mulcahy et al., 2018, 2020). The atmosphere has 85 vertical levels up to 85km, and a 1.875° longitude by 1.25° latitude resolution.

The Community Earth System Model, version 2 (CESM2; Danabasoglu et al., 2020) is a state-of-the-art, fully-coupled Earth system model with prognostic atmosphere, ocean, land, sea ice, land ice, river runoff, and wave components developed by the U.S. National Science Foundation's National Center for Atmospheric Research. The model is run at a horizontal resolution of 1.25° longitude x 0.9° latitude. The atmospheric component used for these simulations is the Whole Atmosphere Community Climate Model (WACCM6; Gettelman et al., 2019), which uses a finite-volume dynamical core and uses 70 vertical levels, up to approximately 140 km. This configuration, CESM2(WACCM6), hereafter CESM2-WACCM, contributed to Phase 6 of the Climate Model Intercomparison Project (CMIP6; Eyring et al., 2016) and has been extensively used to model SAI (e.g. Tilmes et al., 2020; Richter et al., 2022). The configuration uses version 4 of the Modal Aerosol Module (MAM4; Liu et al., 2016), which features prognostic aerosol representation and represents sulfate aerosols in Aitken, accumulation, and coarse modes. The ocean component is version 2 of the Parallel Ocean Program (POP2; Smith et al., 2010; Danabasoglu et al., 2012, 2020), and the land component is version 5 of the Community Land Model (CLM5; Lawrence et al., 2019).

The Energy Exascale Earth System Model version 3 (E3SMv3) is developed by the U.S. Department of Energy (DOE) and is a fully coupled earth system model with five components for the atmosphere, land, river, ocean, and sea ice (Golaz et al., 2025). This is the first use of E3SMv3 for simulations of SAI. Previous versions of E3SMv2 and E3SMv2-PA (Brown et al., 2024) have been validated against the Mount Pinatubo eruption (Brown et al., 2024; Hu et al., 2025) and used for simulations of SAI (Wheeler et al., 2025). E3SMv3 is run with three different horizontal grids for the atmosphere, ocean and sea ice, and land and river components. For the simulations in this paper, the 'ne30pg2_r05_IcoswISC30E3r5' grid is used. The 'ne30pg2_r05_IcoswISC30E3r5' grid includes a cubed-sphere grid with a spacing of $\sim$110 and $\sim$165 km for the atmosphere dynamics and physics grids, an unstructured horizontal grid with 20-30 km resolution for the ocean and sea-ice components, and a 0.5° regular latitude-longitude grid for the land and river components (Golaz et al., 2025). The atmosphere component is the E3SMv3 atmosphere model (EAM; Xie et al., 2025), which has improved vertical resolution in the lower stratosphere with 80 vertical levels (up to approximately 60 km) relative to E3SMv2 (Golaz et al., 2022). Prognostic aerosols are simulated with the Modal Aerosol Module with Prognostic Stratospheric Aerosol (MAM5-SPA) which includes a prognostic sulfate aerosol scheme for stratospheric coarse sulfate particles into MAM4 (Hu et al., 2025). The ocean component is MPAS-Ocean ((Smith et al., 2025; Golaz et al., 2025) and the land component is the E3SMv3 land model (ELMv3; Golaz et al., 2025).

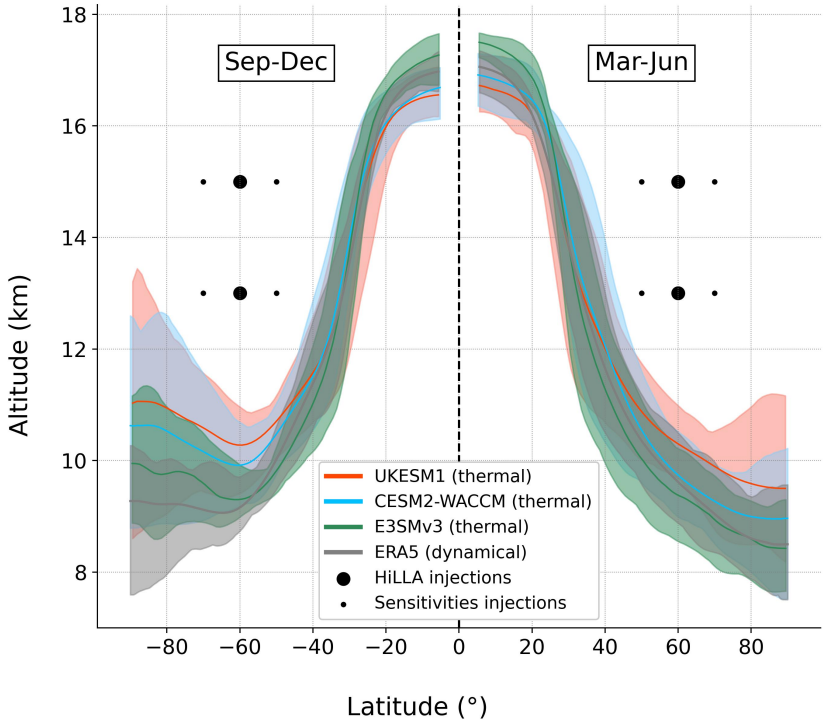

Figure 1. Tropopause altitude in UKESM1, CESM2-WACCM, E3SMv3 and the ERA5 reanalysis, as well as the locations of the HiLLA-13 and HiLLA-15 simulations, and 3-year sensitivities. Tropopause values shown are the time means over the final 25 years of the historical scenario (1991-2015) for UKESM1 and CESM2-WACCM and the same period for ERA5. For E3SMv3, which had no historical scenario available, the time period is 2035-2050. Shaded regions show the minimum-maximum range of the monthly tropopause height over the four months during the 25-year period. The tropopause definition for models is the World Meteorological Organization (WMO) 1st thermal tropopause, and for ERA5 is the dynamical.

2.2 Simulations

The specifications for all simulations are shown in Table 1. The injection locations in latitude/altitude space are shown in Figure 1, along with the tropopause position as modelled in UKESM1, CESM2-WACCM, E3SMv3, and in the ECMWF Reanalysis version 5 (ERA5) (Hersbach et al., 2020), with zonal mean tropopause height data taken from Hoffmann and Spang (2022). We designed a sensitivity suite to test the response to changes in injection strategy for HiLLA scenarios. Across these simulations we vary injection altitude, latitude, seasonality, and longitude. All simulations are run under the background SSP2-4.5 emissions pathway (O'Neill et al., 2016), the SSP emissions scenario which most closely matches current policies (Hausfather, 2025). Our simulations initiate in 2035, branching from SSP2-4.5 by injecting a fixed magnitude of 12 Tg SO_2 per year in total, following the same protocol used for low-latitude high-altitude injections in Visioni et al. (2023). The rate of

injection varies across the simulations to keep the total annual injection constant, given the varying injection period between three and five months in each hemisphere per year.

There are two central HiLLA scenarios which serve as the baseline SAI scenarios against which we compare the shorter sensitivity simulations: HiLLA-13 and HiLLA-15, each of which run for 35 years. These inject SO_2 for 4 months in the Northern Hemisphere spring/early-summer (March-June) and 4 months in the Southern Hemisphere (September-December). HiLLA-13 and HiLLA-15 inject at 13 km and 15 km, respectively, at 60° North and South. The '13 km' and '15 km' heights by which we label the simulations are nominal only. In UKESM1, which operates on hybrid-height vertical coordinates, the vertical resolution at 13-15 km is approximately 600 m, and the SO_2 is injected into grid boxes injected which have centres at 12.9 and 15.4 km, respectively. In CESM2-WACCM, injections are into grid cells bounded by pressure surfaces at 12.9-13.0 km for HiLLA-13, and at 14.7-14.9 km for HiLLA-15. In E3SMv3, the injection grid cells are bounded at 12.5-13.5 and 14.5-15.5 km altitudes, with centers exactly at the nominal altitudes. A single ensemble member is run for each simulation, and all simulations branch from the same member of SSP2-4.5. In UKESM1 this SSP2-4.5 simulation is 'r1i1p1f2', in CESM2-WACCM it is 'r1i1p1f1', and in E3SMv3 a novel control simulation following the SSP2-4.5 scenario was simulated. We refer to this background run as 'r1' in each case. For UKESM1 and CESM2-WACCM, we also show the ensemble range and mean in figures below, but in E3SMv3 only a single control member is available.

In addition to the two central HiLLA scenarios, we also simulated nine short (3-year duration) simulations in each model. Across these nine simulations, we independently vary the injection latitude, altitude, seasonality (within the spring/early summer strategy previously shown to be significantly more effective (Lee et al., 2021)), and longitude. We do not attempt to fully explore this four-dimensional injection scenario space, but instead vary each feature independently, relative to our central HiLLA cases, to show a first-order estimate of the sensitivity to each.

We also use the ARISE-SAI-1.5 (hereafter "ARISE") simulations, in CESM2-WACCM (Richter et al., 2022) and UKESM1 (Henry et al., 2023), as a comparison representing low-latitude high-altitude (i.e. "conventional") SAI. These simulations use injection of SO_2 at 15°N/S and 30°N/S, and at approximately 21km, with the injection at each latitude controlled by a feedback algorithm targeting the meridional pattern of temperature response, as well as the global mean temperature. See Richter et al. (2022) for a full description of the ARISE scenario. The comparison of our HiLLA scenarios against ARISE is imperfect, since here we do not control the injection to achieve the same outcome state. While we reduce the impact of this difference by scaling effects by unit cooling or injection, it is still an important limitation to our study. The upcoming G6-1.5K-HiLLA simulations will allow for analyses not subject to this limitation, since they will be directly comparable against G6-1.5K-SAI simulations which will achieve the same global temperature target via an alternative strategy (Visioni et al., 2024, 2025).

3 Results

3.1 Temperature response

The global, polar, and tropical near-surface air temperature evolution under the background SSP2-4.5 and the central HiLLA-13 and HiLLA-15 scenarios, in each model, are shown in Figure 2. Given the large magnitude of injection (12 Mt in total) from

Table 1. Overview of the simulations used in this study. The central cases were run for 35 years, while sensitivity cases were run for 3 years to assess the impact of varying parameters. Month ranges are inclusive in all cases, i.e. MAMJ/SOND means injection in for four months March-June in the Northern Hemisphere, and four months September-December in the Southern Hemisphere. Due to an error in the injection settings, E3SMv3 does not have output for the 2nd seasonality sensitivity simulation, with injection in MAMJJ/SONDJ.

Label	Altitude (km)	Latitude (°N/S)	Months	Longitude (°)	Length (years)
Central cases					
HiLLA-13	13	60	Mar-Jun (MAMJ)/ Sep-Dec (SOND)	180	35
HiLLA-15	15	60	Mar-Jun (MAMJ)/ Sep-Dec (SOND)	180	35
Sensitivities					
Latitude					
	13	70	Mar-Jun (MAMJ)/ Sep-Dec (SOND)	180	3
	13	50	Mar-Jun (MAMJ)/ Sep-Dec (SOND)	180	3
Altitude					
	15	70	Mar-Jun (MAMJ)/ Sep-Dec (SOND)	180	3
	15	50	Mar-Jun (MAMJ)/ Sep-Dec (SOND)	180	3
Seasonality					
	13	60	Mar-May (MAM)/ Sep-Nov (SON)	180	3
	13	60	Mar-Jul (MAMJJ)/ Sep-Jan (SONDJ)	180	3
	13	60	Feb-Jun (FMAMJ)/ Aug-Dec (ASOND)	180	3
Longitude					
	13	60	Mar-Jun (MAMJ)/ Sep-Dec (SOND)	0	3
	15	60	Mar-Jun (MAMJ)/ Sep-Dec (SOND)	0	3

year one of deployment, decreases in Global and Arctic temperature beyond the 5-member ensemble range of the SSP2-4.5 simulations happen within the first few years (Figure 2). In the Antarctic, the internal variability in temperature is larger and so the cooling signal takes longer to emerge. Figure 2 also demonstrates the lower efficiency and more polar cooling profile of HiLLA-SAI which means that despite the large magnitude of injection used here, cooling in the Tropics equates to only a several decade delay of warming under SSP2-4.5. The HiLLA-13 case produces approximately 0.6°C of global mean cooling (Figure 3), which is reached after around 10 years of deployment (Figure A1) under the constant injection magnitude used in this scenario. More precisely, UKESM1, CESM2-WACCM and E3SMv3 see 0.58°C, 0.70°C and 0.64°C of global mean cooling over the final 20 years of the simulation (2050-2069), respectively. Raising the altitude of injection to 15 km increases the global cooling over the final 20 years to 0.92°C, 0.93°C, and 1.04°C in UKESM1, CESM2-WACCM and E3SMv3 (these values are increases of 60%, 34% and 62% relative to the 13 km case, respectively).

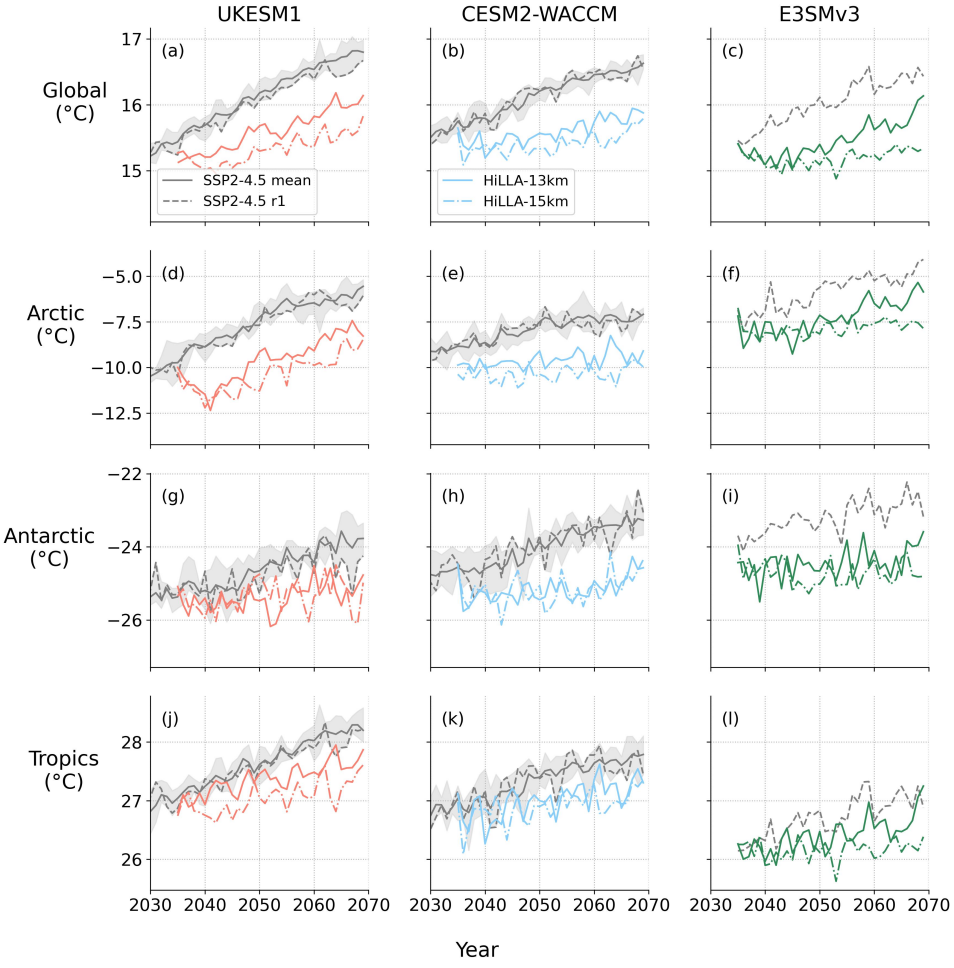

Figure 2. Global, Arctic (>66°N), Tropics (23°S-23°N) and Antarctic (>66°S) near-surface air temperature evolution under the background SSP2-4.5 scenario (grey) and the HiLLA-13 and HiLLA-15 scenarios (colours), in UKESM1 (a, d), CESM2-WACCM (b, e) and E3SMv3 (c, f). HiLLA-13 is represented by the solid colored lines and HiLLA-15 by the dash-dotted lines. 'r1' refers to the first ensemble member of the SSP2-4.5 scenario, from which the HiLLA simulations branch, and is shown by the grey dashed line. The SSP2-4.5 ensemble mean (first five members) is shown by the solid grey line and the range across these members by the shaded grey region. At the time of writing, the E3SMv3 SSP2-4.5 ensemble data was not available, so we compare against a single control run starting at 2035 in this case.

The HiLLA-SAI cases produce a polar focused cooling profile (Figure 4). The feedbacks which drive Arctic amplification (see above) mean that even low-latitude SAI produces more absolute temperature change in the Arctic than in the global mean (Henry et al., 2024). However, the greater Arctic cooling is particularly strong for HiLLA scenarios, which show 3.8 (UKESM1), 2.7 (CESM2-WACCM), and 2.4 (E3SMv3) times more Arctic (>66°N) than global mean cooling, for the 13 km injection case (Figure 5). Part of the inter-model difference in this Arctic to Global cooling ratio can be explained by the relative

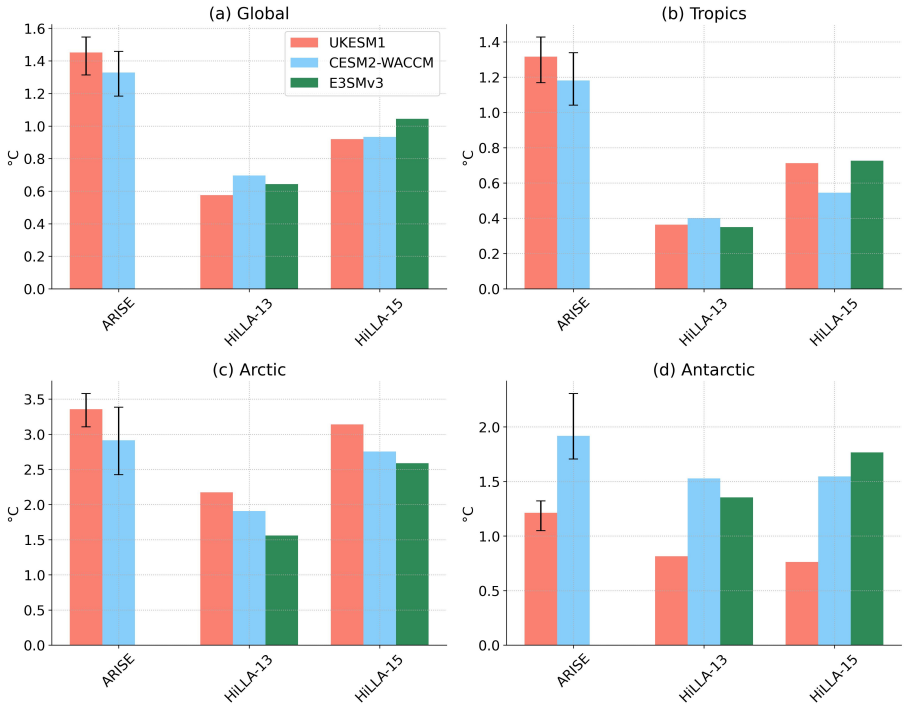

Figure 3. Regional cooling efficiencies. For HiLLA cases, the change in near-surface air temperature in the annual and spatial mean is plotted for each region relative to the background simulation (SSP2-4.5 ensemble mean) over the final 20-years of simulation. For ARISE, the same quantity is used except that in this case, the cooling is scaled linearly to match the 12 Mt /year injection magnitude of the HiLLA cases, and the difference is taken as the ensemble mean of ARISE (5 members in both cases) against the 5 members of SSP2-4.5 from which these runs branch. Error bars for ARISE indicate the ensemble range across the 5 members. The 'Tropics', 'Arctic' and 'Antarctic' are defined as (23°S-23°N), >66°N, and >66°S, respectively.

Arctic amplification ratios of the models (3.2, 1.8, and 2.6) under SSP2-4.5. However, this is not the complete explanation, since CESM2-WACCM has a smaller Arctic amplification ratio than E3SMv3 under warming, but a higher Arctic to Global cooling ratio under HiLLA-13. The regional temperature changes per degree global temperature change for all scenarios, models and regions are shown in Figure 5. The HiLLA-15 case has a similar ratio of Arctic to global mean cooling to the HiLLA-13 case, with ratios of 3.4, 3.0 and 2.5, for UKESM1, CESM2-WACCM and E3SMv3, respectively. In the Antarctic, there are larger model differences in cooling (Figure 3). In particular, UKESM1 has a weak cooling response to both HiLLA-13 and HiLLA-15 in the Antarctic, of approximately 50% of the equivalent cooling in CESM2-WACCM. Neither UKESM1 nor CESM2-WACCM show an increase in Antarctic cooling under 15 km injection relative to 13 km, unlike for every other region assessed (and unlike E3SMv3).

Both UKESM1 and CESM2-WACCM have been used to simulate the ARISE-1.5K scenario, hereafter "ARISE", (Richter et al., 2022; Henry et al., 2023), which is useful for comparison of the regional cooling pattern under HiLLA scenarios to global

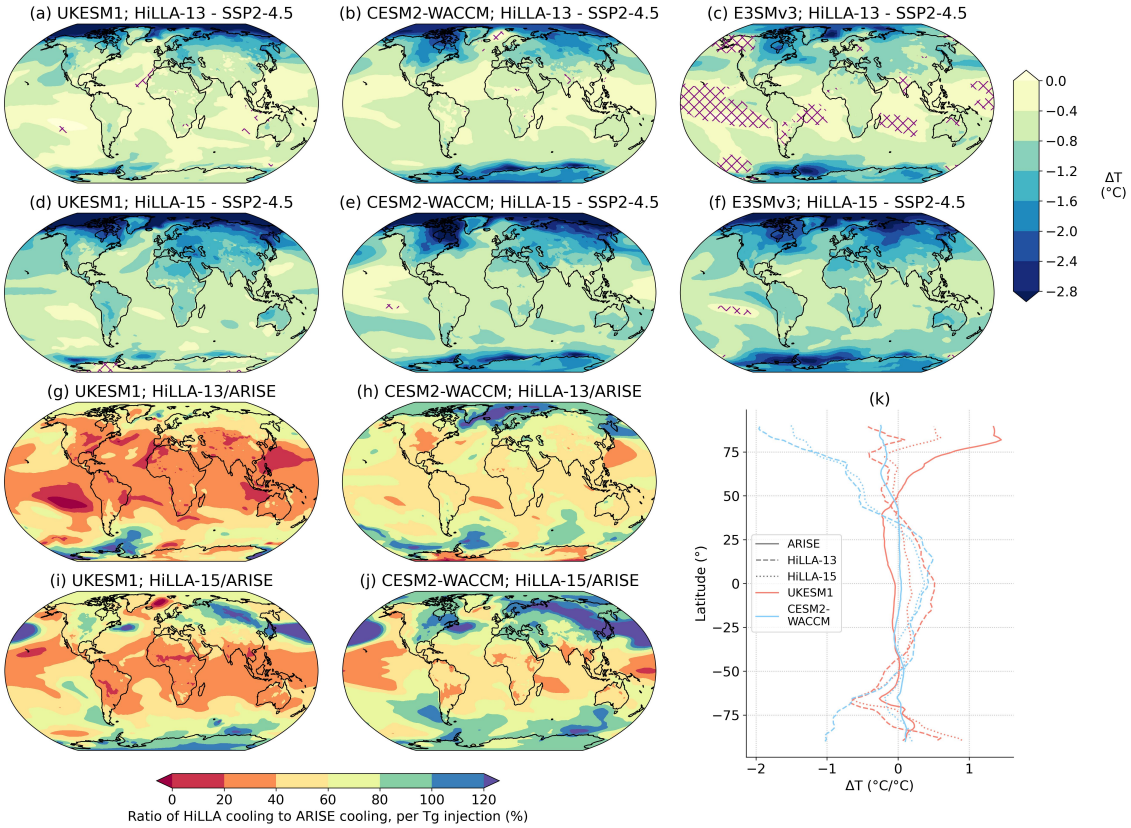

Figure 4. Spatial pattern of temperature change under HiLLA simulations. Panels (a) - (f) show the near-surface air temperature change relative to the background simulation, SSP2-4.5, over the final 20-years (2050-2069) of each HiLLA simulation. Purple hashing marks changes which are not significant at a 5% False Discovery Rate, following Wilks (2016), using Welch's two sample t-test. E3SMv3 has only a single SSP2-4.5 member to compare against, meaning larger changes are needed for significance in this case. Panels (g) - (j) show the Ratio of cooling under HiLLA to that under ARISE-1.5K. 'Cooling' in both cases refers to the change in temperature relative to SSP2-4.5 over the period 2050-2069, and is normalized by the injection magnitude in each case. Panel (k) shows the zonal mean change in temperature relative to the 20-year period under SSP2-4.5 with the same temperature as that achieved under SAI over the period 2050-2069 (i.e. relative to the "target state"), normalized by the total global mean cooling under SAI.

feedback-controlled SAI scenarios. Figure 4 shows the result of this comparison, with the cooling in ARISE scaled linearly to the injection magnitude (12 Mt SO_2/year) used under the HiLLA strategies. The efficiency of cooling is lower than that of the ARISE scenario over most regions of the globe for both the 13 km and 15 km HiLLA cases. HiLLA-SAI is much less
190 efficient than ARISE in the tropics and sub-tropics. With injection at 13 km, almost all regions equatorward of 40° see less than 40% of the ARISE efficiency in both UKESM1 and CESM2-WACCM. The average efficiency relative to ARISE over the tropics (23°S-23°N) is 28% in UKESM1 and 33% in CESM2-WACCM. However, HiLLA-SAI achieves efficiencies of cooling comparable to or greater than ARISE over much of the high latitudes under the 15 km injection case.

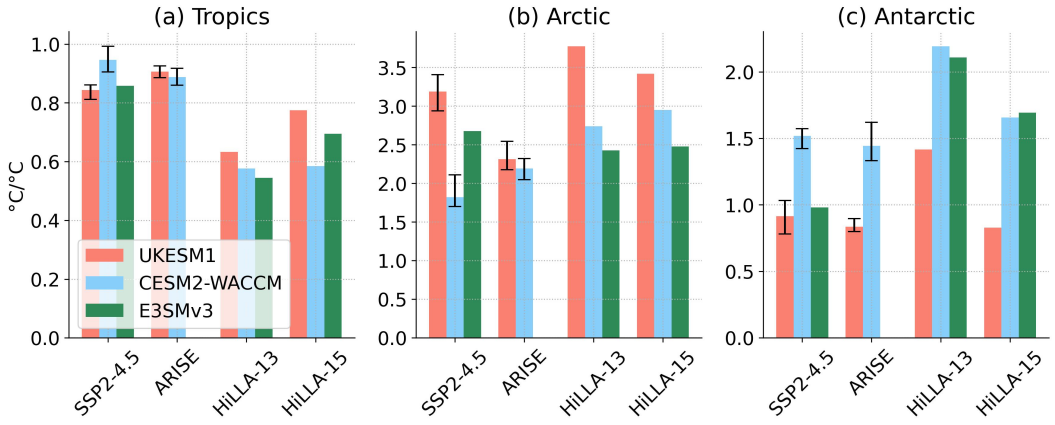

Figure 5. Regional temperature change per unit global mean temperature change, for the Tropics (23°S-23°N), Arctic (>66°N), and Antarctic (>66°S). Changes are relative to the background SSP2-4.5 scenario over [2050-2069] for the SAI scenarios. For SSP2-4.5 the temperature changes are [2050-2069] - [2015-2035] for UKESM1 and CESM2-WACCM. For E3SMv3, the SSP2-4.5 control run begins in 2035, and so we take the change [2060-2069] - [2035-2045].

The reduced tropical cooling under HiLLA-SAI represents a combination of, first, reduced global mean cooling efficiency and, second, a more polar cooling profile. Of these, the former effect is larger. The tropical temperature change per unit global temperature change is approximately two thirds as large under HiLLA-13 as the equivalent ratio under SSP2-4.5, as shown in Figure 5 – specifically, it is 75%, 61% and 64% of this value for UKESM1, CESM2-WACCM and E3SMv3, respectively. Whereas the global mean cooling efficiencies under HiLLA-13 in UKESM1 and CESM2-WACCM are 40% and 52% of their respective values under ARISE. The reduced tropical cooling efficiency under HiLLA-SAI is less pronounced if the injection altitude is increased to 15 km in UKESM1 and E3SMv3, but not in CESM2-WACCM. Under HiLLA-15, the values for tropical cooling per unit global cooling are 92%, 62%, and 81% of each model's equivalent ratio under SSP2-4.5 warming, for UKESM1, CESM2-WACCM and E3SMv3, respectively. That is, in UKESM1, HiLLA-15 cools the tropics at 92% of the rate relative to the global mean cooling which would be needed to offset SSP2-4.5 warming, given sufficient injection magnitude. In CESM2-WACCM however, HiLLA-15 sees the same ratio of tropical to global cooling as HiLLA-13, but increases the absolute tropical cooling due to the higher efficiency of global cooling per unit injection relative to HiLLA-13.

The large differences between UKESM1 and CESM2-WACCM in the zonal temperature changes relative to the nominal 'target' state arise, at least in part, from differences in the meridional pattern of warming in these two models. UKESM1 has strong Arctic amplification of warming, which is not fully offset with injection at 30°N under the ARISE scenario (Henry et al., 2023). Whereas CESM2-WACCM has less strong background Northern Hemisphere high latitude warming, in part due to a strong North Atlantic warming hole (and associated decline in the Atlantic Meridional Overturning Circulation), which is not present in UKESM1 (Henry et al., 2023).

Given the strong seasonality of injection (and forcing), we also consider the seasonality of the temperature change under the HiLLA scenarios. The SAI forcing peaks in local mid-/high-latitude summer in each hemisphere, so we might expect stronger

cooling in local summer than local winter, and a consequent reduction in both the local strength of the seasonal cycle outside the tropics, and the absolute interhemispheric temperature difference. However, as shown in Figure A2, the simulated response of the seasonal cycle amplitude varies strongly by latitude. In the Arctic where faster warming in the winter than summer is decreasing the annual seasonal cycle, HiLLA-SAI acts to partially restore that greater seasonal cycle with cooling (due to the larger absolute cooling in winter, see Section 3.4). A similar effect is seen in the sub-polar Antarctic. However, there is a decrease in the strength of the seasonal cycle in the northern hemisphere mid-latitudes, and in the high southern latitudes, particularly in CESM2-WACCM. We do not plot this metric for E3SMv3 due to a lack of the needed historical simulation data.

Similarly, we can also assess the seasonality of the interhemispheric temperature difference, that is, the average Northern minus average Southern Hemisphere temperature, in a given month. We might expect summer-peaking forcing from SAI to reduce the amplitude of the seasonality in interhemispheric temperature difference, but the models do not simulate this (Figure A3). While the maximum (positive) interhemispheric temperature difference, during Boreal summer, is reduced, the minimum (largest negative value) during Austral summer is increased in magnitude (i.e. made more negative), such that the overall amplitude is within the range of the SSP2-4.5 ensemble. Put more simply, the absolute value of Northern Hemisphere cooling during its local winter is larger than the Southern Hemisphere cooling during its local summer, offsetting the reduction in seasonality which would otherwise be expected from the larger Northern Hemisphere cooling during its local summer. The implications of this for tropical precipitation are discussed in Section 3.6.

3.2 Aerosol distribution and optical depth

The seasonal cycle of zonal mean aerosol optical depth (AOD) distribution produced under the HiLLA-13 and HiLLA15 scenarios in each model is shown in Figure 6. This AOD pattern demonstrates that HiLLA-SAI produces a polar-peaking and highly seasonal aerosol burden and forcing. This seasonality is strongest in the 13 km case, which sees close to zero H_2SO_4 burden in the several months leading up to the deployment start in each hemisphere (Figures A4 and A5 show the full monthly evolutions of zonal H_2SO_4 burden in UKESM1 and CESM2-WACCM). Aerosol burdens on levels were not saved in E3SMv3, so Figure 7 shows results only for UKESM1 and CESM2-WACCM. While the highest concentrations of sulfate occur at the poles, there is also equatorward and upward transport (Figure 7). Considering the total sulfate burden in each latitude band (i.e. accounting for area) makes this clear. The sulfate burden measured as mass per degree latitude peaks equatorward of injection, at 50-60° N/S (Figure 8). The majority of total additional atmospheric sulfate burden is equatorward of the 60° N/S injection locations in both UKESM1 and E3SMv3 (60 - 75%, depending on scenario, model and hemisphere). The larger burden equatorward of the injection sites is not inconsistent with a poleward mean flow; it could be explained by a greater average lifetime of sulfate which is mixed equatorwards, given the reduced downwelling at lower latitudes.

We now decompose the global cooling per unit injection into two components: the global mean AOD per unit injection, and the global mean cooling per unit global mean AOD. This separates the effects of variation in aerosol lifetime and size distribution (which define the AOD per unit injection) from the effects of variation in the combination of SW forcing per unit AOD and temperature sensitivity to that global mean forcing, which together define cooling per unit global mean AOD (Kleinschmitt et al., 2018; Zhang et al., 2024; Duffey et al., 2025a). The resulting values for the three models under the HiLLA

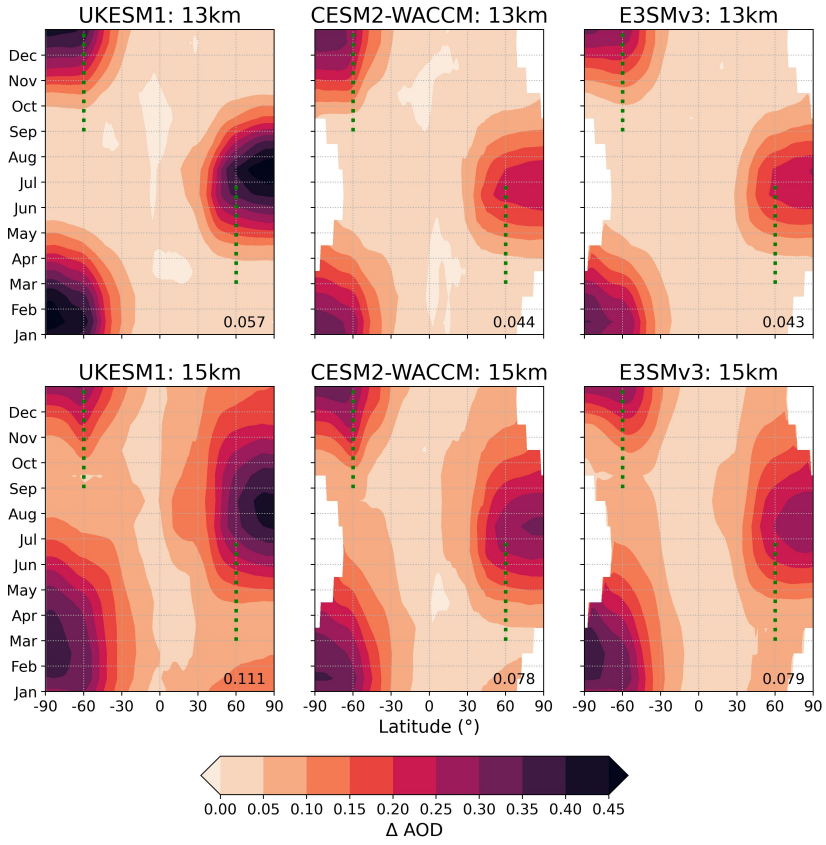

Figure 6. Zonal mean total column AOD at 550nm. The difference relative to the background scenario, by month, averaged over the final 20 years of each simulation (2050-2069), is shown. Note that for CESM2-WACCM and E3SMv3, the 'AODVIS' variable is used, which is only outputted where insolation is non-zero, causing the data gaps in the polar winter. The green dotted lines show the injection locations and months.

scenarios, along with ARISE for comparison where available, are shown in Figure 9. The AOD per unit injection is larger in UKESM1 than the other two models (panel a), but the reduced change in global temperature per unit AOD in UKESM1 (panel b) largely cancels this effect, so that the overall cooling per unit injection (panel c) is less varied between the three models.

Variation in AOD per unit injection arises from a combination of variation in aerosol lifetime (and therefore burden) and of variation in size distribution (and therefore AOD per unit burden). Here, the higher AOD per unit injection in UKESM1 is likely driven by UKESM1's smaller aerosol size (Figure A6), since UKESM1 also has lower SO_4 burden per unit injection than the other models (Figures 7 and 8). The cause of the lower global mean cooling per unit AOD in UKESM1 than the other two models (which is not seen in the ARISE simulations) is not clear, but may be related to the weak Antarctic cooling under HiLLA scenarios in UKESM1 (Figure 2).

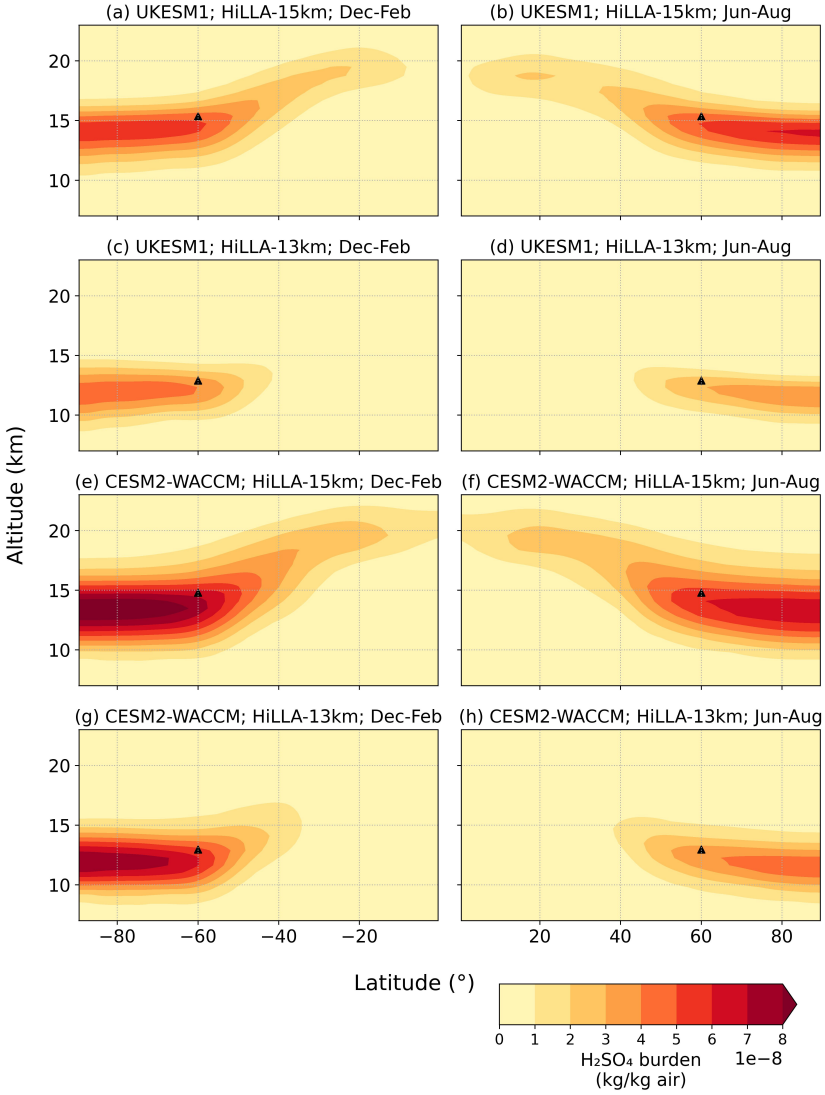

Figure 7. Zonal and seasonal mean burden of H_2SO_4 mass-mixing ratio (kg per kg air), in UKESM1 (a-d) and CESM2-WACCM (e-h), averaged over the final 20 years of each simulation (2050-2069). Black triangles indicate the injection locations in each case. The top row (a, b) shows response under HiLLA-15, and the bottom row (c, d) under HiLLA-13 km. The left hand column (a, c) shows the Austral summer (Dec-Feb inclusive) burden, and the right column shows the Boreal summer burden (Jun-Aug inclusive). CESM2-WACCM burdens, which are outputted from the model in units of SO_4, were converted to H_2SO_4 mass-mixing ratio for comparison with UKESM1. The monthly SO_4 concentrations in E3SMv3 outputs were only recorded on individual isobaric surfaces and so are not included here.

Compared to the ARISE scenario, the HiLLA scenarios result in more global cooling per unit AOD, by up to a factor of 2 (for HiLLA-13 in CESM2-WACCM). This greater cooling efficiency per unit AOD offsets part of the lower AOD per unit injection relative to ARISE, reducing the difference in global cooling efficiency between the scenarios. It is caused by the seasonality

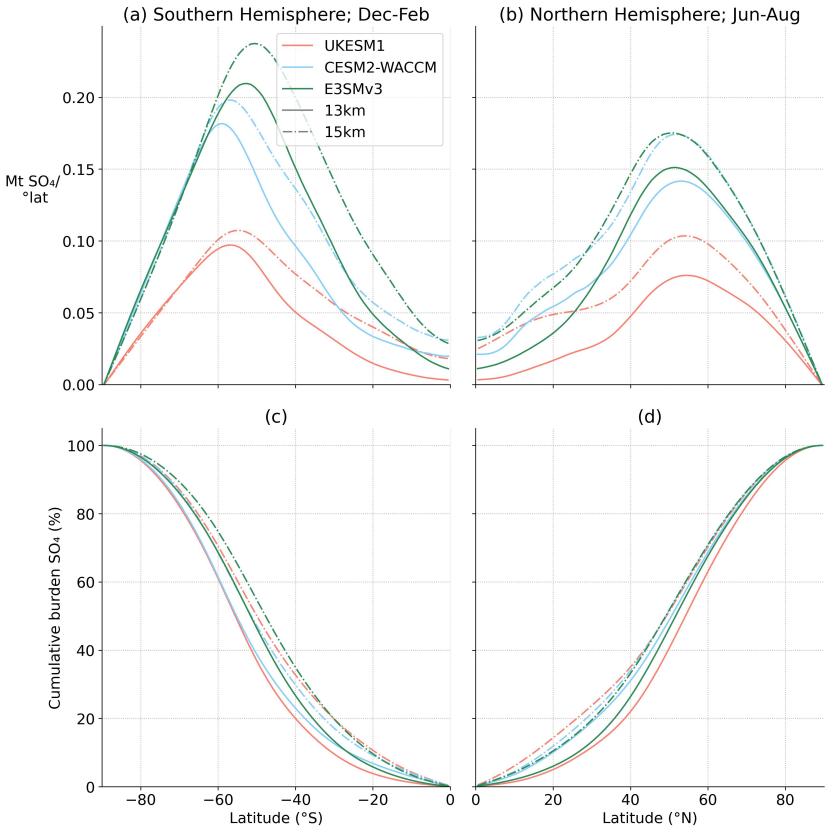

Figure 8. Total additional burden of atmospheric SO_4 per degree latitude relative to SSP2-4.5, for the Southern Hemisphere (a), and Northern Hemisphere (b), in local summer in each case, under the HiLLA-13 and HiLLA-15 scenarios. Cumulative additional burdens, shown as a fraction of the hemispheric total, summing from the equator, are shown in (c) and (d). Note that no continuity is expected at the equator in (a) and (b), since different seasons are shown in the two subplots.

of the injection and the resulting AOD, which means the AOD produced coincides with greater insolation, combined with feedbacks in the polar regions (particularly the Arctic) which amplify the temperature response to the local forcing (e.g. Pithan and Mauritsen, 2014).

3.3 Sensitivity to injection strategy

In addition to the two central cases, for which we present 35-year simulations, we also simulate a set of nine 3-year simulations, from which we can assess the sensitivity of AOD to the injection latitude, altitude, longitude and seasonality. We focus our assessment on the response of AOD to these features, because it stabilises at values within internal variability of the decadal mean under the 35-year simulations by the third year of injection.

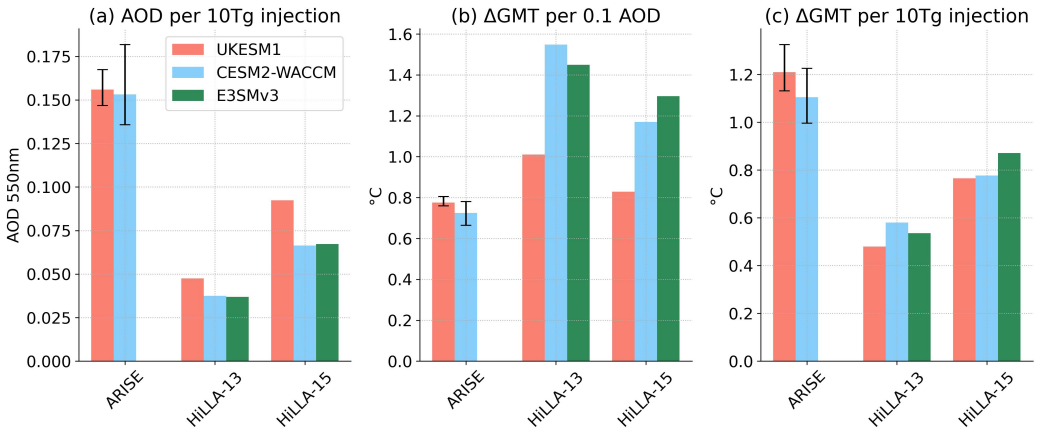

Figure 9. Decomposition of cooling efficiency into (a) change in global mean AOD per 10 Tg of SO_2 injection, (b) change in global mean temperature ('cooling') per 0.1 change in global mean AOD, and (c) change in global mean temperature per 10 Tg injection. (c) is the product of (a) and (b). The HiLLA scenarios are compared against the ARISE-SAI-1.5 scenario in UKESM1 and CESM2-WACCM.

The sensitivity of global mean AOD to altitude of injection, with injection latitude at 60°N/S, can be seen in the contrast between the HiLLA-13 and HiLLA-15 scenarios throughout this study. The three models show roughly a factor of two increase in mean AOD change in both hemispheres with the additional 2km of injection height (Figure 10). This difference is larger than the difference in SO_4 burden between HiLLA-13 and HiLLA-15. For example, in UKESM1, the Northern Hemisphere AOD under HiLLA-15 is 202% of the HiLLA-13 value, but the total burden of SO_4 is 136% of the HiLLA-13 value (see Figure A7). The higher AOD per unit burden under HiLLA-15 in UKESM1 is likely due to the larger particle size under this strategy, which takes the effective radius closer to the optimal for scattering at around 300 nm (Dykema et al., 2016). The aerosol effective radius in UKESM1 and CESM2-WACCM under the two HiLLA scenarios is shown in Figure A6 (the data to produce the effective radius in E3SMv3 was not saved). The maximum effective radius under HiLLA-15 in UKESM1, approximately 250 nm, is around half the 500 nm maximum in CESM2-WACCM. The CESM2-WACCM values are similar to those reported by Bednarz et al. (2023a), for this model under their polar injection scenario.

The impact of varying injection latitude between 50 and 70°N/S on the resulting AOD is smaller than for variation in altitude, and is not consistent between the models (Figure 10). For example, at 15 km injection, moving the latitude from 60° to 50° increases the resulting AOD by 19% in UKESM1, leaves it unchanged in CESM2-WACCM, and decreases it by 29% in E3SMv3. Varying the injection longitude between of 0° and 180° (at 60° N/S and 13/15 km) has a smaller impact (Figure 11), although there may be a small gain in efficiency by injecting at 180° (i.e. over the Bering Sea rather than the Norwegian Sea in the Northern Hemisphere). Similarly, within the spring/early-summer injection regime, the influence of further fine-tuning of the seasonality of injection is generally small and is inconsistent across the models (Figure 11). In the Southern Hemisphere, AOD is higher for September-December (SOND) injection in UKESM1, but in the other models, variation is within the year-to-year variability (one standard deviation) of the SOND value. In the Northern Hemisphere, where AOD differences between

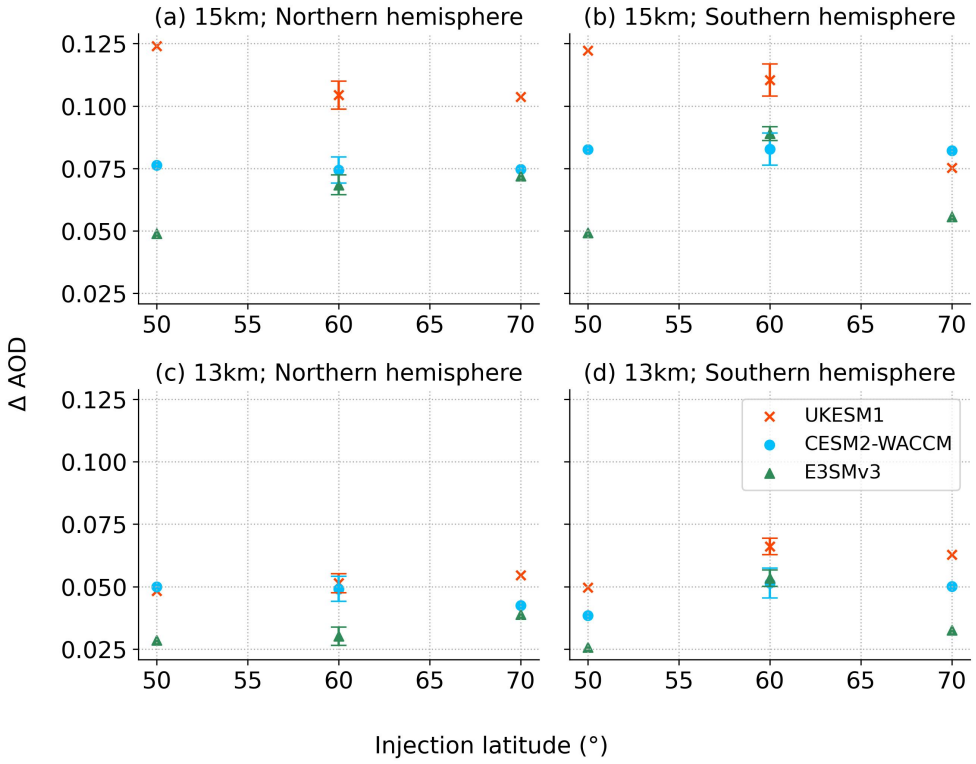

Figure 10. Change in total atmospheric column aerosol depth (AOD) from background scenario (SSP2-4.5) under injection at 15 km (a, b) and 13 km (c, d) and varying latitude. All values are for the third year of these (3-year) simulations. All runs here have longitude 180°E, and seasonality MAMJ/SOND. Values shown are hemispheric means for the (a,c) Northern Hemisphere and (b, d) Southern Hemisphere. The uncertainty range shown for the 60° injection cases is one standard deviation of the year-to-year variability, derived from the 35-year HiLLA experiments.

the models are larger, the longer injection season of February-June (FMAMJ) results in higher mean AOD in UKESM1 and E3SMv3, but March-June (MAMJ) is marginally higher in CESM2-WACCM.

3.4 Arctic Amplification and the Seasonality of Arctic Cooling

Given the strong amplification of Arctic warming with its marked Autumn/Winter peak (e.g. Rantanen et al., 2022), it is of interest to examine the seasonality of the Arctic cooling response to HiLLA-SAI. The local Arctic forcing under SAI drops to zero in the Winter months when there is no insolation – or can be positive if injecting throughout the year due to longwave absorption by the sulfate aerosols (Lee et al., 2021; Duffey et al., 2025a) – but the late autumn and winter months (particularly November and December) see the largest absolute Arctic temperature change under both HiLLA-SAI and ARISE (Figure 12). This result concurs with previous simulations (e.g. Lee et al., 2023a). It suggests that the same drivers which cause Arctic

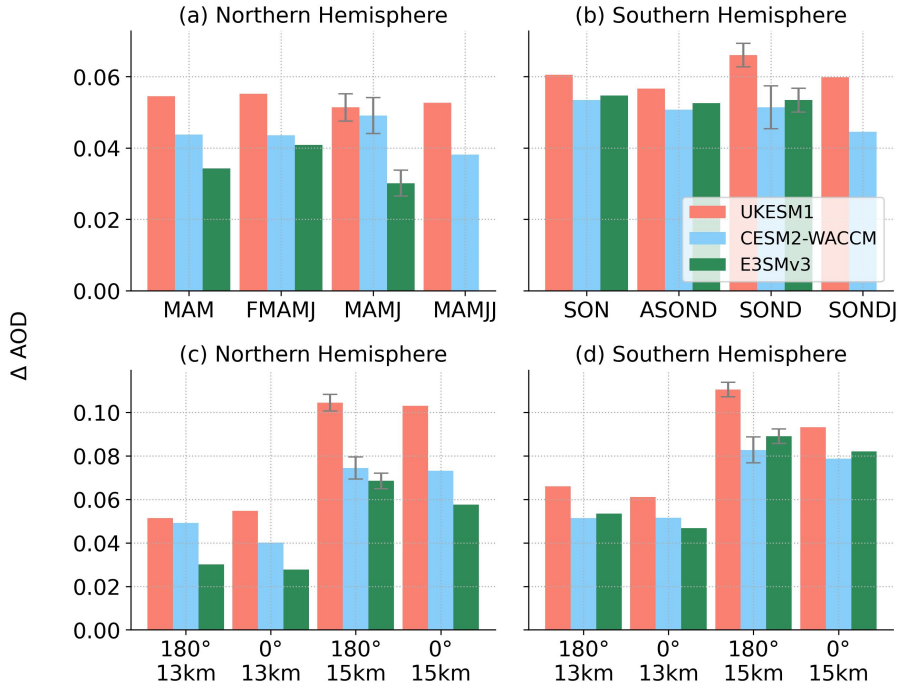

Figure 11. Change in total atmospheric column aerosol depth (AOD) from background scenario (SSP2-4.5) under varying seasonality (a, b) and longitude (c, d). Values shown are hemispheric means for the (a, c) Northern Hemisphere and (b, d) Southern Hemisphere. The uncertainty range shown for the 180°E cases is one standard deviation of the year-to-year variability, derived from the 35-year HiLLA-SAI experiments. Panels (a) and (b) show the impact of varying longitude of injection from 180°E (the default in our HiLLA scenarios) to 0°E, under injection at 13 and 15 km. All values are for the third year of these short (3-year) sensitivity simulations. All runs in (a) and (b) have latitude of injection at 60°N/S and seasonality MAMJ/SOND. Panels (c) and (d) show the impact of varying the precise seasonality of injection relative to the central case (March-June, MAMJ). All runs in panels (c) and (d) use injection at 60°N/S, 180°E, 13 km. No E3SMv3 data is available for the MAMJJ/SONDJ case, due to a mistake in injection settings for this simulation.

Amplification of warming to peak in the Winter – including the lapse rate feedback and ocean heat fluxes (Pithan and Mauritsen, 2014; Hahn et al., 2021; Duffey et al., 2025b) – also apply for cooling under SAI.

While the absolute cooling under HiLLA-SAI peaks in Winter, this peak is weaker than the peak in winter-time warming. As such, HiLLA-SAI overcools the Arctic summer, and undercools the winter, in the sense that if HiLLA-SAI was deployed to offset a given annual mean Arctic warming, there would be positive residual warming in winter and negative residual warming in summer (Figure 12, right column). That is, HiLLA-SAI is reducing the strength of the Arctic temperature seasonal cycle relative to a baseline with equal annual mean temperature, even though it increases the seasonal cycle relative to the background warming scenario (Figure A2). This finding was previously shown for the Geoengineering Large Ensemble Project (GLENS) simulations by Jiang et al. (2019) and also applies for the ARISE scenario in UKESM1 and CESM2-WACCM (Figure 12). The seasonal temperature residuals shown in Figure 12 are, in almost all months, larger under HiLLA-SAI than under ARISE,

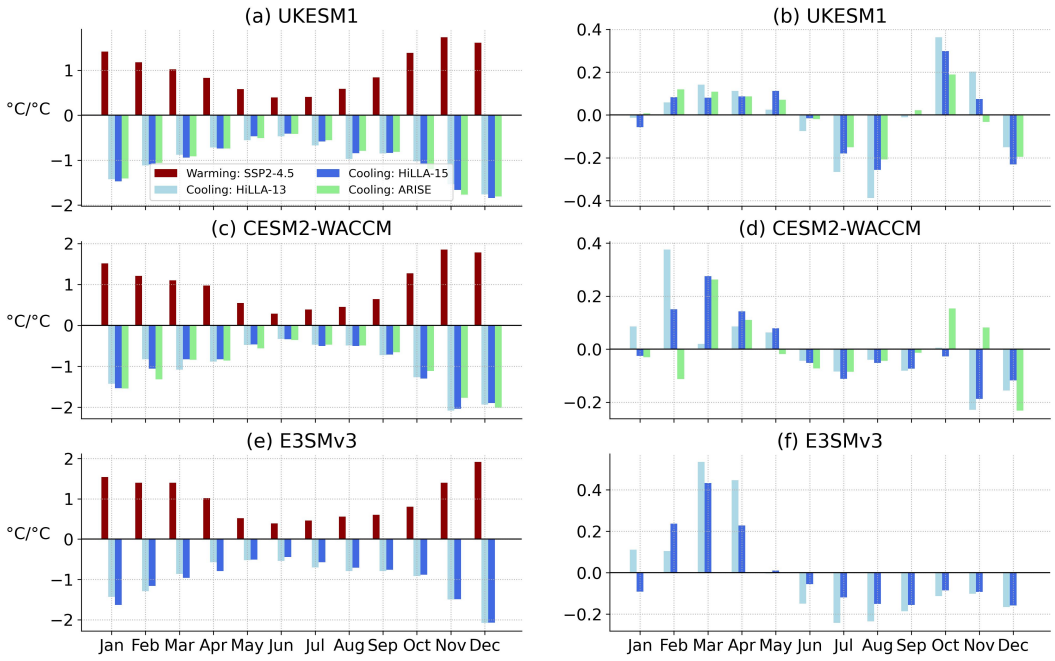

Figure 12. Seasonality of Arctic (>66°N) warming and SAI cooling. The left hand side plots (a, c, e) show Arctic warming (SSP2-4.5 2050-2069 - pre-industrial), and cooling (SAI scenario - SSP2-4.5, 2050-2069), for the three models. Values are normalized by the annual mean change. The right column plots (b, d, f) show the residuals (warming + cooling) from the left side plots.

meaning this reduction in seasonality relative to the target state is larger under the more seasonal and polar forcing of the HiLLA strategy.

3.5 Sea-ice response

Local temperature is a strong control on total Arctic and Antarctic sea-ice cover (e.g. Ridley et al., 2012) and SAI simulations consistently show increases in both Arctic and Antarctic sea-ice area relative to the background warming scenario (Kravitz et al., 2013; Berdahl et al., 2014; McCusker et al., 2015; Jones et al., 2018; Jiang et al., 2019; Lee et al., 2021, 2023a; Goddard et al., 2023). As such, it is not surprising to see that sea-ice area is increased in both the winter maximum and summer minimum in both hemispheres and in all models under HiLLA-SAI (Figure 13). All three models share similar trends in sea ice area response to SAI. In the Arctic, the September minimum sea ice is increased relative to SSP2-4.5 as is the March maximum. Generally, the increases are greater for the HiLLA-15 cases than HiLLA-13. However, UKESM1 and CESM2-WACCM have much stronger increases in September sea ice than E3SMv3. UKESM1 shows a dramatic initial increase in September sea ice to the first decade of SAI which declines steeply starting in 2045 to nearly ice-free by 2070. CESM2-WACCM shows a similarly strong initial response but has a much shallower decline in September sea ice area through 2070. CESM2-WACCM, sees an ice-free Arctic by the 2040s under SSP2-4.5, but has around 4 Mkm^2 of September sea-ice area under HiLLA-15 and

around 3 Mkm^2, approximately the observed 2024 value (Fetterer et al., 2025), under HiLLA-13 in the 2060s. E3SMv3 has a much smaller increase in September sea ice area, which remains near or below ice free under both SSP2-4.5 and SAI. The impact on the Arctic March maximum area is smaller across the models, particularly in CESM2-WACM and E3SMv3, for which the background decline in the winter maximum under SSP2-4.5 is small.

For Antarctic sea ice, all models show an increase in February and September Antarctic sea ice response to SAI. Unlike for Arctic sea ice, E3SMv3 shows a similar magnitude increase in sea ice area to UKESM1 and CESM2-WACCM with SAI. As with the temperature impacts, and unlike the Arctic response, there is little difference in the Antarctic February sea-ice minimum response to HiLLA-13 versus HiLLA-15. Both strategies increase the Antarctic February minimum sea-ice area in all models, with the response in CESM2-WACCM (of $\sim$2.5 Mkm^2) around twice the size of that in the other two models, but no model shows a clear increase in the response for the 15 km injection case relative to the 13 km. However, the additional injection height produces a stronger sea-ice increase for the Antarctic September sea ice maximum.

Temperature is the principal driver of Arctic sea ice change (Notz and Stroeve, 2018), and CMIP6 models consistently show a linear decline in annual minimum sea ice area with temperature (Notz and Community, 2020). In our HiLLA simulations, Arctic annual mean temperature is a good predictor of the sea ice area at both annual minimum and maximum, suggesting that the relationship between local temperature and pan-Arctic sea ice cover which applies under the background SSP2-4.5 scenario also holds under SAI (Figure A8). The Antarctic sea ice area is plotted against local temperature in Figure A9. In the Antarctic case, atmospheric circulation is a stronger control on interannual variability of sea ice (e.g. Blanchard-Wrigglesworth et al., 2021), and the relationship between local annual mean temperature and sea-ice area is weaker.

3.6 Precipitation

The global precipitation response under HiLLA-15 is shown in Figure 14 (see Figure A10 for the 13 km injection case). Our simulations are not sufficient in duration or number of ensemble members to present a detailed assessment of the impact on regional precipitation given its large internal variability. With our 20-year assessment for one ensemble member, most regional changes do not meet a 5% false discovery rate significance threshold (Wilks, 2016), particularly at sub-annual timescales. However, a general reduction in precipitation relative to the background (warmer) SSP2-4.5 scenario is evident, particularly in the high latitudes, where the changes are significant in the annual mean in all three models across most of the Arctic and Antarctic. This reduction in high-latitude precipitation relative to the control is expected given the strong cooling in these regions, and given the increase in precipitation with warming which is simulated under SSP2-4.5 for the Arctic (e.g. McCrystall et al., 2021) and Antarctic (e.g. Bracegirdle et al., 2020).

One potential impact of HiLLA-SAI which we seek to examine here is a reduction in local summer rainfall in low latitude regions on either side of the equator, associated with a reduced amplitude of Intertropical Convergence Zone (ITCZ) seasonal migration due to stronger cooling in the summer hemisphere. By analogy to the ITCZ shifts associated with asymmetric SAI forcing (Haywood et al., 2013), such an effect might be hypothesised given the seasonal migration of the ITCZ towards the warmer hemisphere, combined with the HiLLA scenarios' summer hemisphere-only AOD pattern. No clear evidence of this effect is seen in the rainfall changes across the three models, although the significant drying during boreal summer in central

Figure 13. Sea-ice area under HiLLA-SAI simulations and SSP2-4.5, by region and minimum/maximum months, for each model. The shaded region for SSP2-4.5 is the ensemble range, the solid line is the ensemble mean, and the dashed line is the first member, from which the HiLLA scenarios branch. 'Arctic' here refers to all sea ice in the Northern Hemisphere, and 'Antarctic' refers to all sea ice in the Southern Hemisphere.

355 Africa in UKESM1 and CESM2-WACCM could be suggestive of this mechanism. However, this is only assessed from a short timeseries, which is inadequate to detect anything but very large precipitation changes given the internal variability. As such, tropical precipitation changes under HiLLA scenarios will require assessment in longer scenarios controlling for global temperature, and with more ensemble members, before any firm conclusions can be drawn.

3.7 Other impacts: sulfur deposition and stratospheric ozone

360 Once the overall increased stratospheric aerosol burden is stable, the global additional magnitude of sulfur deposition is equal to the injected mass. The global cooling efficiency reduction for HiLLA-SAI compared to high-altitude strategies described

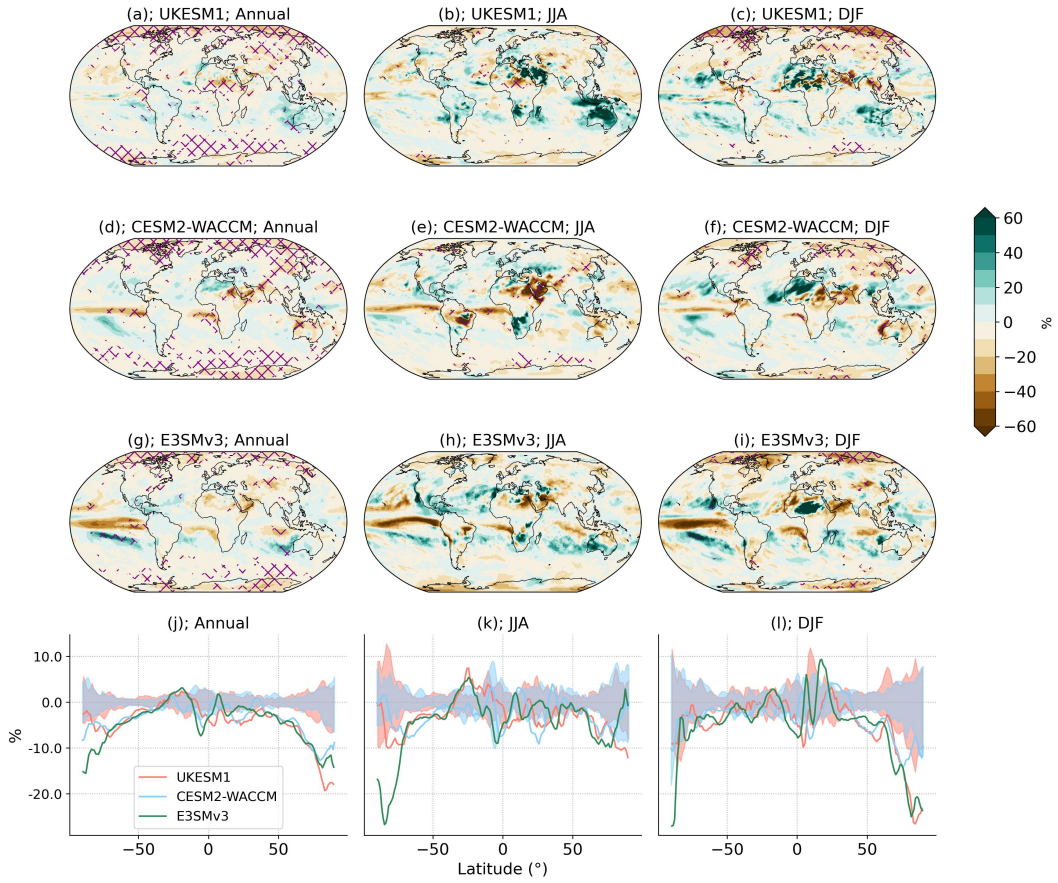

Figure 14. Change in precipitation under HiLLA-15 relative to SSP2-4.5 over the period 2050-2069. Maps (a-i) show grid cell changes, over the 20 years of assessment, relative to the ensemble mean of the SSP2-4.5 simulation (10 members each for UKESM1 and CESM2-WACCM, but only 1 member for E3SMv3), as a percentage of the local SSP2-4.5 precipitation. Purple hashing marks changes which are significant at a 5% False Discovery Rate, following Wilks (2016), using Welch's two sample t-test. The single SSP2-4.5 member for E3SMv3 means a larger signal is required for significance in this case. Zonal mean plots are also shown (j-l), as a percentage change from the SSP2-4.5 ensemble mean. For UKESM1 and CESM2-WACCM, the 10-member ensemble range in variation of the 20-year mean is shaded.

above therefore implies an increase in overall deposition per unit of cooling of a factor of 2-2.5 for HiLLA-13, relative to high-altitude low-latitude injection strategies such as ARISE. If we compare against ARISE on a per unit injection basis, the total deposition must be the same, but the regional patterns can differ. Figure A11 shows the zonal mean SO_4 deposition in UKESM1 and CESM2-WACCM (data to support this analysis was not saved in the E3SMv3 simulations). Overall, the zonal patterns under HiLLA-SAI are similar to those under ARISE, although with greater mid/high-latitude Northern Hemisphere deposition (and less mid/high-latitude Southern Hemisphere deposition) in CESM2-WACCM than ARISE (which injects mostly in the Southern Hemisphere in this model), and with somewhat higher sub-polar Southern Hemisphere deposition in UKESM1. Maps of the change in deposition relative to the background SSP2-4.5 scenario are shown in Figure A12. We see from these maps

that, first, the largest absolute deposition values occur equatorward of injection, but, second, that the largest changes relative to the local background occur over more pristine regions in the high latitudes and the Southern Ocean, particularly Greenland and the Canadian Arctic. This result has also been highlighted under lower-latitude injections (Visioni et al., 2020), in which case the stratospheric circulation moves aerosols towards the mid-to-high latitudes and results in increased deposition in the same areas.

Changes in stratospheric ozone concentrations relative to the SSP2-4.5 background simulation under the HiLLA scenarios are shown in Figure A13. SAI impacts ozone through changes to both chemistry and dynamics (Tilmes et al., 2018, 2021; Bednarz et al., 2023a). Of the three models, only CESM2-WACCM includes heterogeneous chemistry in the stratosphere, and so only this model is expected to capture the depletion due to increased heterogeneous reactions on sulfate aerosols. In this model, decreases of ozone concentration of up to around 30% are found in the Antarctic stratosphere, and significant reductions are also seen in the equatorial lower stratosphere and the Arctic. In the other two models, where only dynamic changes are captured, there are significant increases in ozone concentration in the tropical lower stratosphere, and, in UKESM1, in both polar regions.

4 Discussion and conclusions

In this study, we have presented a first multimodel assessment of HiLLA-SAI, to characterise the global climate response to this form of SAI deployment. HiLLA-15, that is, an annual injection of 6 Mt SO_2 per hemisphere during the local spring and early summer in the subpolar lower stratosphere (at 15 km and 60°N/S) is simulated to reduce global mean temperature by 0.9 - 1.0°C across the three models. Alongside this global cooling, the models show strong polar cooling, an increase in sea-ice area in both hemispheres, a decrease in high-latitude precipitation and an increase in the amplitude of the Arctic seasonal cycle resulting from the greater absolute cooling during the winter months. HiLLA-13, that is, the same SAI scenario but at 13 km injection altitude, shows qualitatively similar impacts but with substantially reduced magnitude – HiLLA-13 achieves ~ 0.6°C of cooling with the same total annual injection of SO_2.

Our modelling suggests that HiLLA deployment, particularly with 15 km injection, could be an effective means of reducing many of the rapid and consequential changes occurring in the Arctic and Antarctic. At the same time, HiLLA-SAI would be a global, not a polar, climate intervention. It would produce cooling, precipitation changes and other regional climate impacts, as well as sulfur deposition, over the entire globe. The majority of the total increase in atmospheric burden is modeled to be equatorward of the 60° N/S injection locations.

We also compared our HiLLA simulations in UKESM1 and CESM2-WACCM against conventional high-altitude low-latitude SAI, which we characterise using the ARISE simulations (Richter et al., 2022). HiLLA-15 achieves approximately equal Arctic cooling efficiency as the ARISE scenario. However, there is strongly reduced cooling efficiency in the low latitudes in HiLLA-SAI relative to conventional high-altitude low-latitude strategies. Under HiLLA-13, the Tropics mean cooling is less than 0.4°C for 12 Mt annual injection in all three models, a local cooling efficiency of around 25% of the ARISE strategy in UKESM1 and CESM2-WACCM. This reduction represents a combination of reduced global mean cooling efficiency and

a more polar cooling profile, and the former effect is larger. While the HiLLA strategies produce a more polar cooling than high-altitude subtropical SAI, this effect is perhaps smaller than sometimes assumed. Across the three models, tropical cooling per unit global cooling under HiLLA-13 is at least 61% of the equivalent ratio under GHG warming, and this ratio increases under 15 km injection in two of three models.

Our simulations suggest that HiLLA-SAI, and therefore SAI using modified existing aircraft rather than newly-developed high-altitude aircraft, is a plausible early-stage deployment option for both polar and global climate intervention strategies. While both 13 km and 15 km injection see meaningful impacts, the higher altitude raises efficiency markedly by increasing the aerosol burden (Figure 7). The three models show close to 1°C more cooling per 12 Mt SO_2 could be achieved in the Arctic, 0.75°C more cooling in the Antarctic, and around 50% greater global mean cooling, under 15 km injection than 13 km. This sensitivity to altitude is important given that 13 km is close to the certified altitude ceiling for large jetliners such as the Boeing 777 which could be used to deliver large payloads with relatively minor modifications (Smith et al., 2024). Our results suggest that using aircraft capable of deploying several km higher than this would strongly increase efficiency for HiLLA strategies.

Varying the latitude of injection between 50° and 70° N/S can make a large difference to resulting hemispheric mean AOD, particularly in the Southern hemisphere. In E3SMv3, injecting at 60°S rather than 50°S at 13 km altitude increases the resulting AOD by around a factor of two. While less extreme in the other two models, all three show an increase in AOD for injection at 60°S relative to 50°S, at 13 km, suggesting that if altitude is limited to this height, then injecting at higher Southern latitudes than the most Southerly airports in Patagonia, at 53-55°S (Smith et al., 2024), would increase efficacy. In the Northern Hemisphere, there is no equivalent increase in AOD with increased latitude from 50° to 60° at 13 km altitude. At the higher altitude of 15 km, there is no consensus between the models on the impacts of that same increase in latitude - in both hemispheres shifting from 50° to 60° increases the resulting AOD E3SMv3 but decreases it in UKESM1, and has no impact in CESM2-WACCM. Future work should explore the drivers of this inter-model difference in the response to variation of injection latitude, particularly as it relates to variation in the models' background lower stratospheric circulation. In general, our results suggest there is limited sensitivity to the longitude and precise seasonality (within the spring/early summer regime) of injection under HiLLA strategies.

Based on the sensitivity analysis presented in this paper, a new experiment, 'G6-1.5k-HiLLA', was designed under the GeoMIP project (Visioni et al., 2025). These simulations follow the HiLLA-15 injection strategy presented here – spring (MAMJ/SOND) injection with equal magnitude at 60° N and 60°S, and at 15 km – but control the total yearly injection magnitude to hold global mean temperature at 1.5K above pre-industrial, defined as the mean global temperature over the period 2020-2039 in each model. G6-1.5K-HiLLA experiment therefore follows the same specification and target as the G6-1.5K-SAI experiment (Visioni et al., 2024; Lee et al., 2025), with the only differences being the injection location and seasonality. As of publication, G6-1.5K-HiLLA simulations have been completed in four earth system models (UKESM1, CESM2-WACCM, E3SMv3 and MIROC-ES2H), and are available online via the Reflective Cloud Hub platform (Duffey, 2026). These new G6-1.5K-HiLLA simulations will allow a first comparison of HiLLA versus low-latitude high-altitude SAI strategies targeting the same temperature outcomes in a multi-model setting.

We have made only a preliminary assessment here of the impacts of HiLLA-SAI on changes in sulfur deposition, stratospheric ozone, and tropical precipitation arising from the polar and seasonal nature of the SAI forcing. There may well be further shortcomings to HiLLA-SAI strategies which our limited simulations here cannot identify. Only one ensemble member was run for each model for each HiLLA strategy here, which limits our analysis, particularly of precipitation responses for which the background variability is large. Additionally, while we assessed two main deployment strategies, as well as the sensitivity to variation in these strategies (Figure 10), this still represents only a narrow window into the total space of possible HiLLA deployments. Future work could usefully broaden this analysis, such as via consideration of dependence on the background emissions scenario, and dependence on injection species. HiLLA strategies produce a more asymmetric pattern of forcing, with forcing alternating between the hemispheres in their respective summer. The consequences of this asymmetry are briefly explored in Figures A2 and A3. These show that despite summer-hemisphere-only forcing, our simulations do not show a suppression of the seasonal cycle of zonal mean temperature (in most latitudes, Figure A2) or the interhemispheric temperature gradient (Figure A3), relative to the SSP2-4.5 background. Future work should assess the broader circulation impacts of summer-hemisphere-only forcing, which are not explored here. Moving beyond the limitations of this analysis to produce a comprehensive assessment of the trade-offs between HiLLA and other SAI strategies, and exploring the processes which drive such differences, is an important near-term goal for the SAI research community.

Code and data availability. All plotting and analysis code is available at https://github.com/alistairduffey/HiLLA_MM and is archived on Zenodo (Duffey, 2025). Data needed to reproduce the analysis is archived on Zenodo (Duffey et al., 2025c). The version of CESM used in this experiment, version 2.1.5, is freely available for download; links to instructions and documentation are available at https://www.cesm.ucar.edu/models/cesm2. E3SMv3 model code can be accessed at https://github.com/E3SMv3-Project/E3SMv3. Additional E3SM model documentation is available at: https://docs.E3SMv3.org/E3SMv3/index.html. The background SSP2-4.5 simulations for UKESM1 and CESM2-WACCM are available from the Earth Sytem Grid Federation, and the NCAR Geoscience Data Exchange (GDEX), respectively.

Appendix A: Supplementary Figures

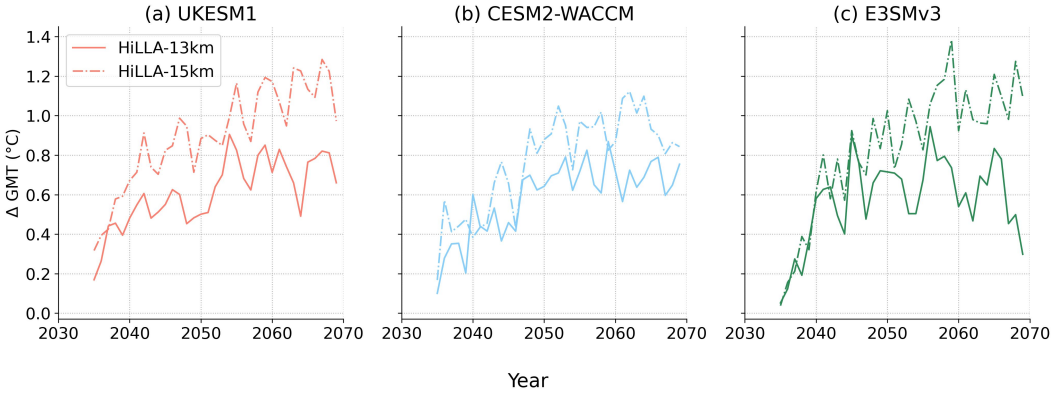

Figure A1. Annual and global mean change in mean near-surface air temperature relative to the background scenario SSP2-4.5, for HiLLA-13 and HiLLA-15 scenarios, in UKESM1, CESM2-WACCM and E3SMv3.

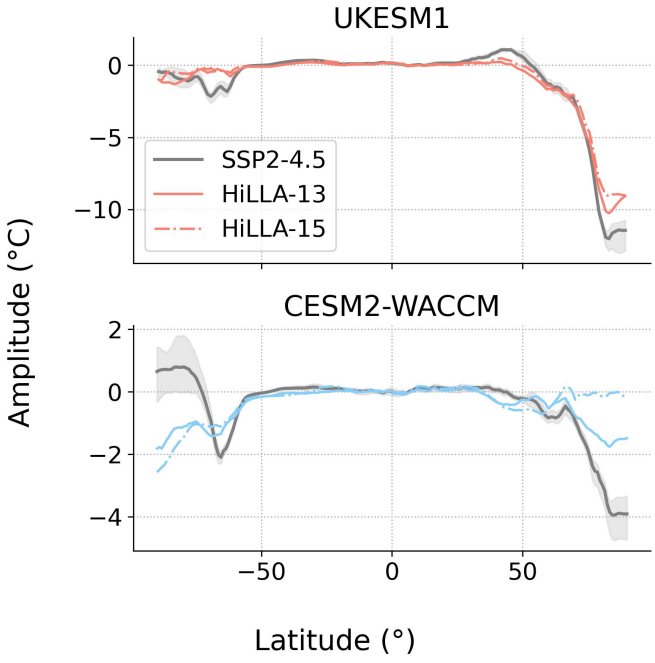

Figure A2. Annual amplitude of the (monthly mean) seasonal cycle, in the zonal mean, for UKESM1 and CESM2-WACCM, SSP2-4.5 (2050-2069) and HiLLA-SAI scenarios (2050-2069). In both cases the amplitude plotted is the anomaly relative to the historical simulation (1995-2015) period. E3SMv3 is not plotted due to lack of simulation availability for the baseline period.

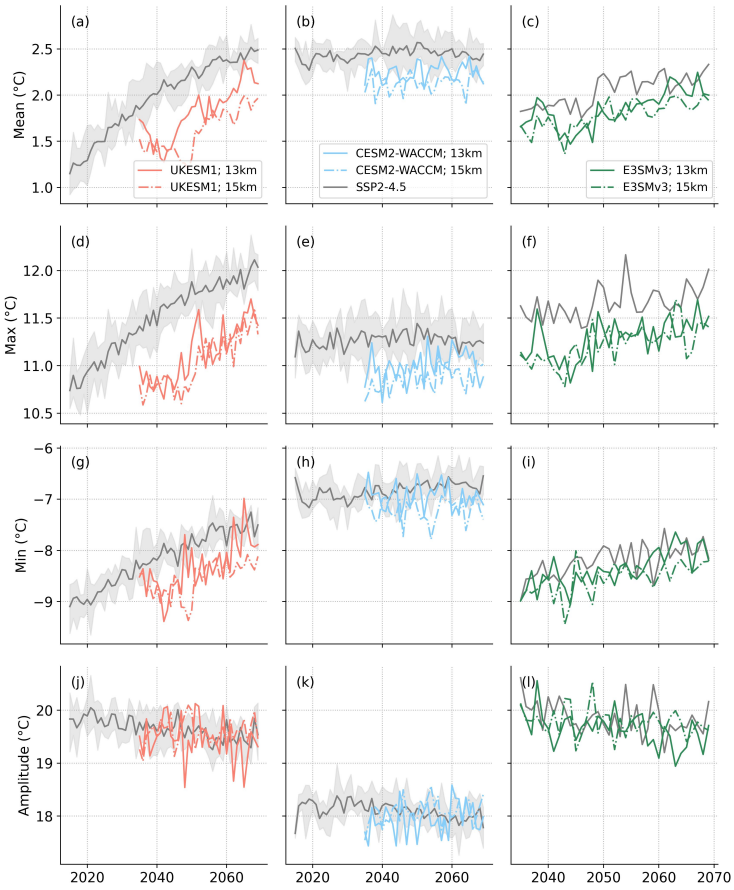

Figure A3. Seasonal cycle of interhemispheric temperature difference. The figure shows the mean (a-c), maximum (d-f), minimum (g-i) and annual amplitude (max - min, j-l) of the interhemispheric temperature difference, defined as the northern hemisphere mean temperature minus the southern hemisphere mean temperature. The seasonal cycle is calculated on the monthly resolution data. The shaded region is the ensemble range over 5 members, for the SSP2-4.5 simulations in UKESM1 and CESM2-WACCM, and the colored lines show the evolution under the HiLLA-15 (dash-dotted line) and HiLLA-13 (solid line) SAI scenarios.

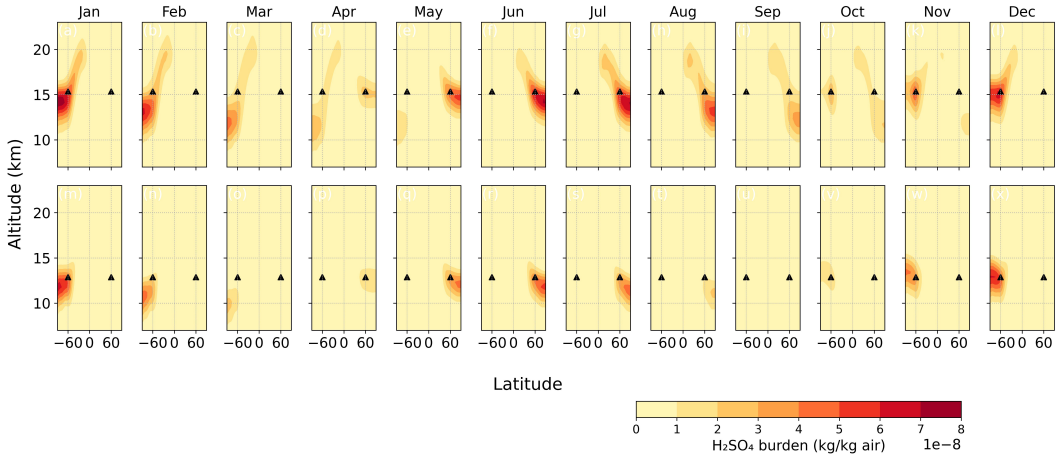

Figure A4. UKESM1 zonal mean monthly burden of H_2SO_4, as a mass-mixing ratio (kg per kg air), averaged over the final 20 years of each simulation (2050-2069). Black triangles indicate the injection locations in each case. The top row (a-l) shows response under HiLLA-15, and the bottom row (m-x) under HiLLA-13.

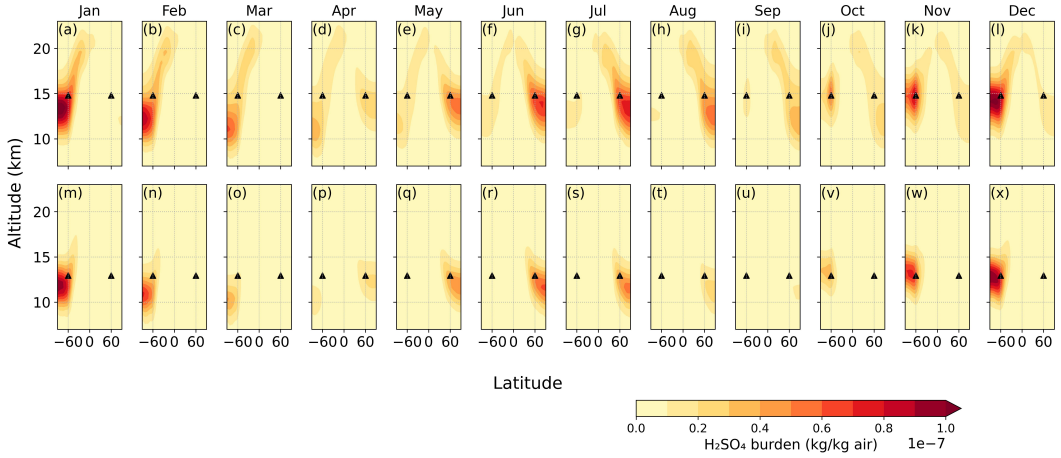

Figure A5. CESM2-WACCM zonal mean monthly burden of H_2SO_4, as a mass-mixing ratio (kg per kg air), averaged over the final 20 years of each simulation (2050-2069). Black triangles indicate the injection locations in each case. The top row (a-l) shows response under HiLLA-15, and the bottom row (m-x) under HiLLA-13.

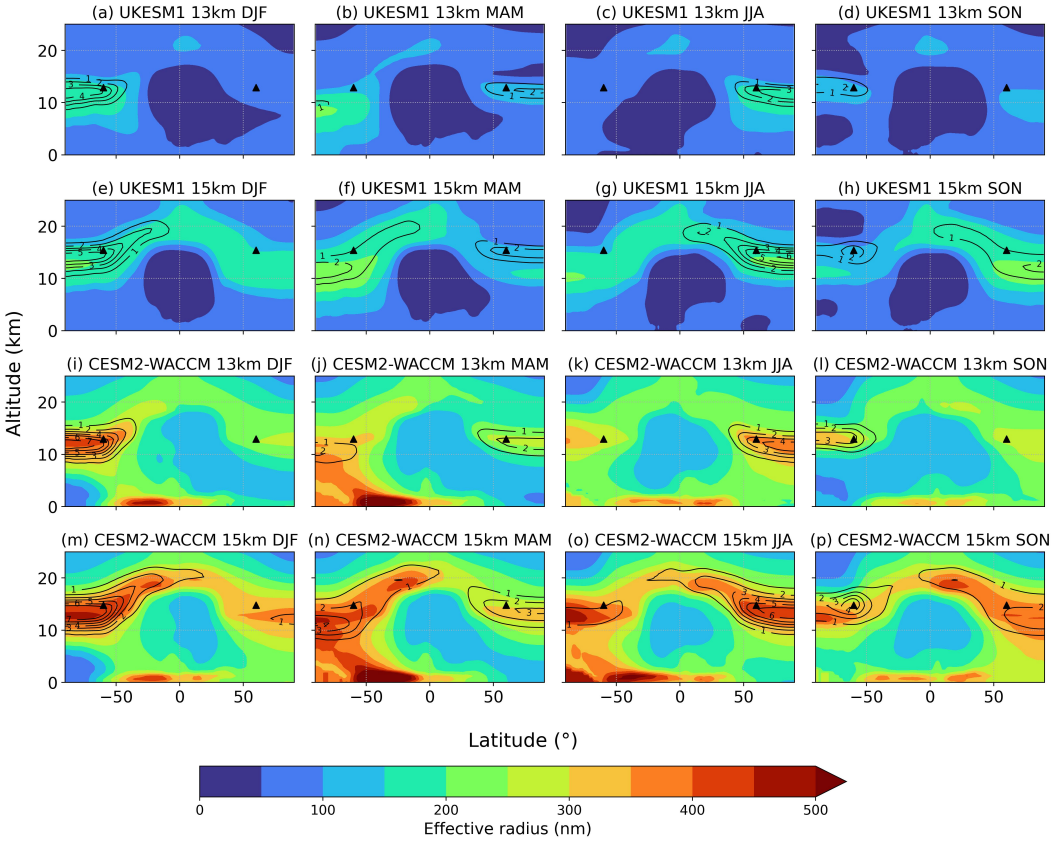

Figure A6. Effective radius of sulfate aerosols in UKESM1 (top) and CESM2-WACCM (bottom) under HiLLA-13 and HiLLA-15, for each season. The mass mixing ratio (10^{-8}kg/kg air) is shown in the contours. All values are the 20-year means over the final 20-years of the simulations (2050-2069). The effective radius for UKESM1, where it is not a direct model output, is calculated as in Visioni et al. (2023). The required geometric standard deviations for each of the four aerosol modes in UKESM1 are given in Walters et al. (2019), and we use a sulfate density of 1769 kg m^{-3} following Mann et al. (2010).

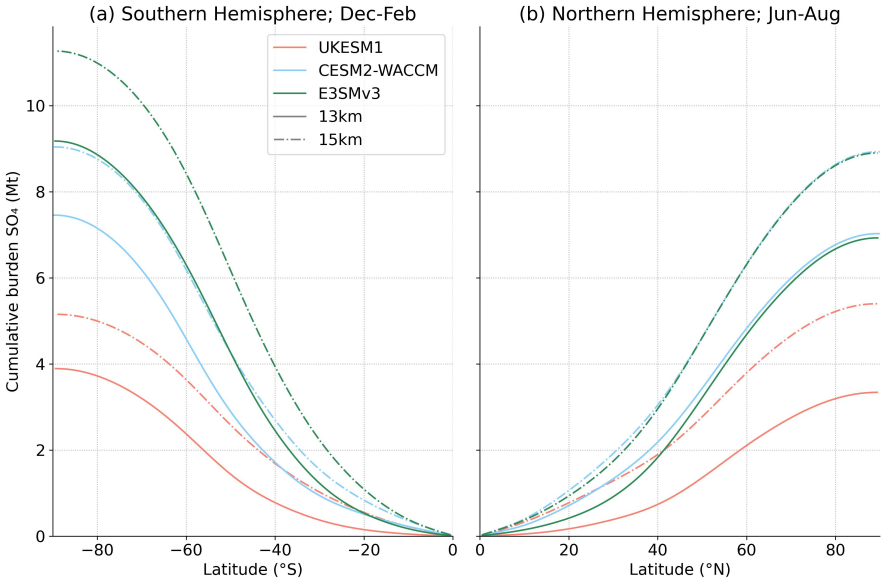

Figure A7. Total additional cumulative burden of atmospheric SO_4 relative to SSP2-4.5, for the Southern Hemisphere (a), and Northern Hemisphere (b), in local summer in each case, under the HiLLA-13 and HiLLA-15 scenarios, summing polewards from the equator.

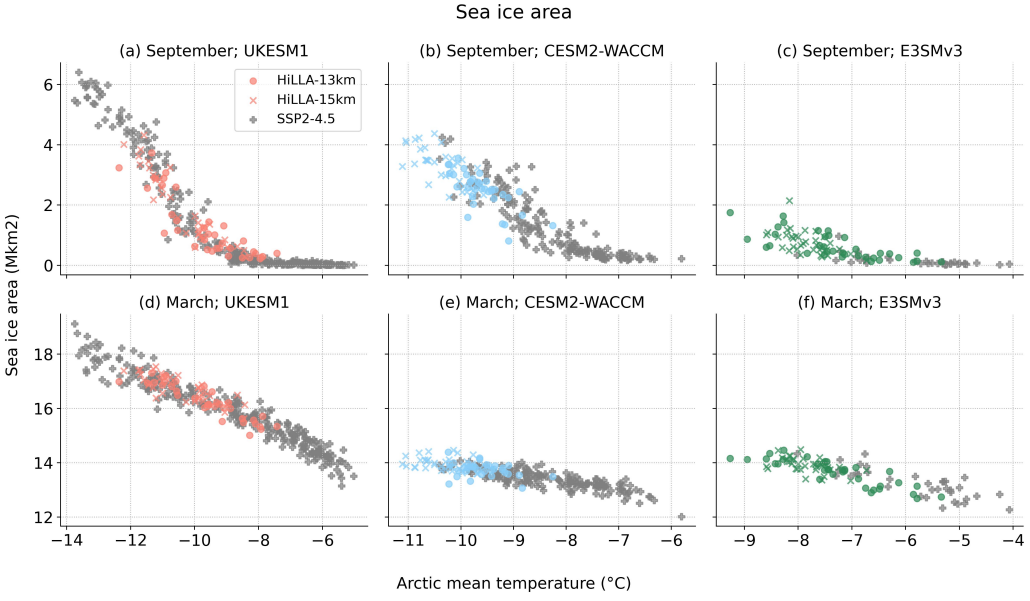

Figure A8. Arctic sea ice area by Month and model, over the HiLLA-SAI and SSP2-4.5 scenarios, plotted against the annual mean Arctic (>66°N) temperature.

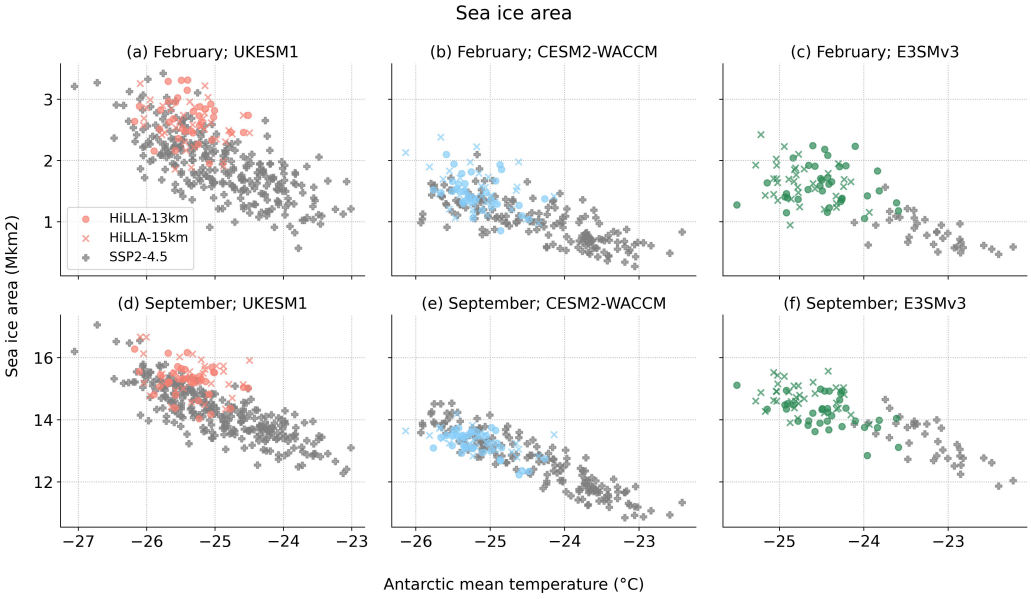

Figure A9. Antarctic sea ice area by Month and model, over the HiLLA-SAI and SSP2-4.5 scenarios, plotted against the annual mean Antarctic (>66°S) temperature.

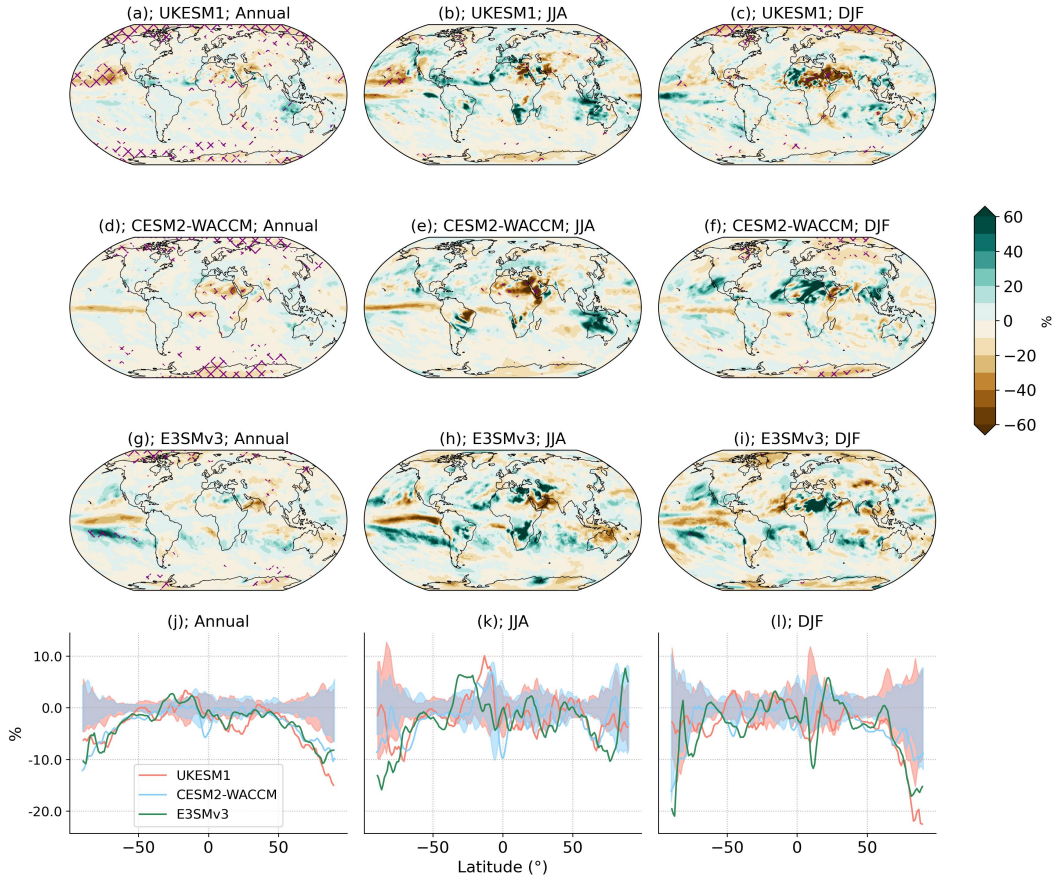

Figure A10. Change in precipitation under HiLLA-13 relative to SSP2-4.5 over the period 2050-2069. Maps (a-i) show grid cell changes, over the 20 years of assessment, relative to the ensemble mean of the SSP2-4.5 simulation (10 members each for UKESM1 and CESM2-WACCM, but only 1 member for E3SMv3), as a percentage of the local SSP2-4.5 precipitation. Purple hashing marks changes which are significant at a 5% False Discovery Rate, following Wilks (2016), using Welch's two sample t-test. The single SSP2-4.5 member for E3SMv3 means a larger signal is required for significance in this case. Zonal mean plots are also shown (j-l), as a percentage change from the SSP2-4.5 ensemble mean. For UKESM1 and CESM2-WACCM, the 10-member ensemble range in variation of the 20-year mean is shaded.

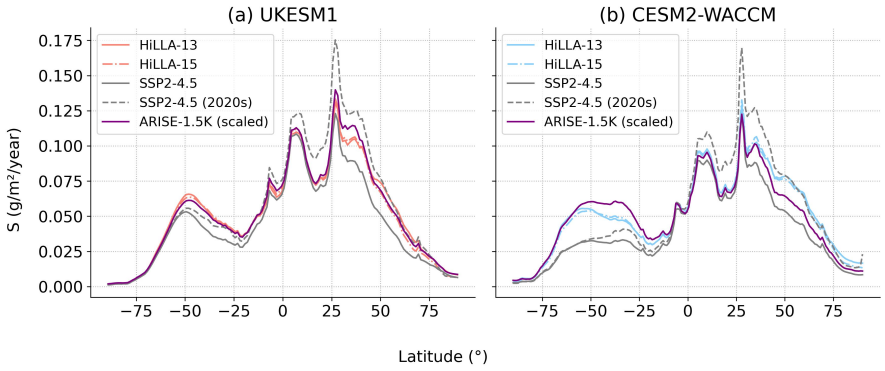

Figure A11. Zonal mean deposition of SO_4, in grams of sulfur, under HiLLA-SAI in UKESM1 and CESM2-WACCM, along with the ARISE deposition, scaled linearly to the same annual injection magnitude (12Mt) as the HiLLA cases. All lines show the 2050-2069 mean except the 'SSP2-4.5 (2020s)' line which shows the present day (2020-2029) simulated value.

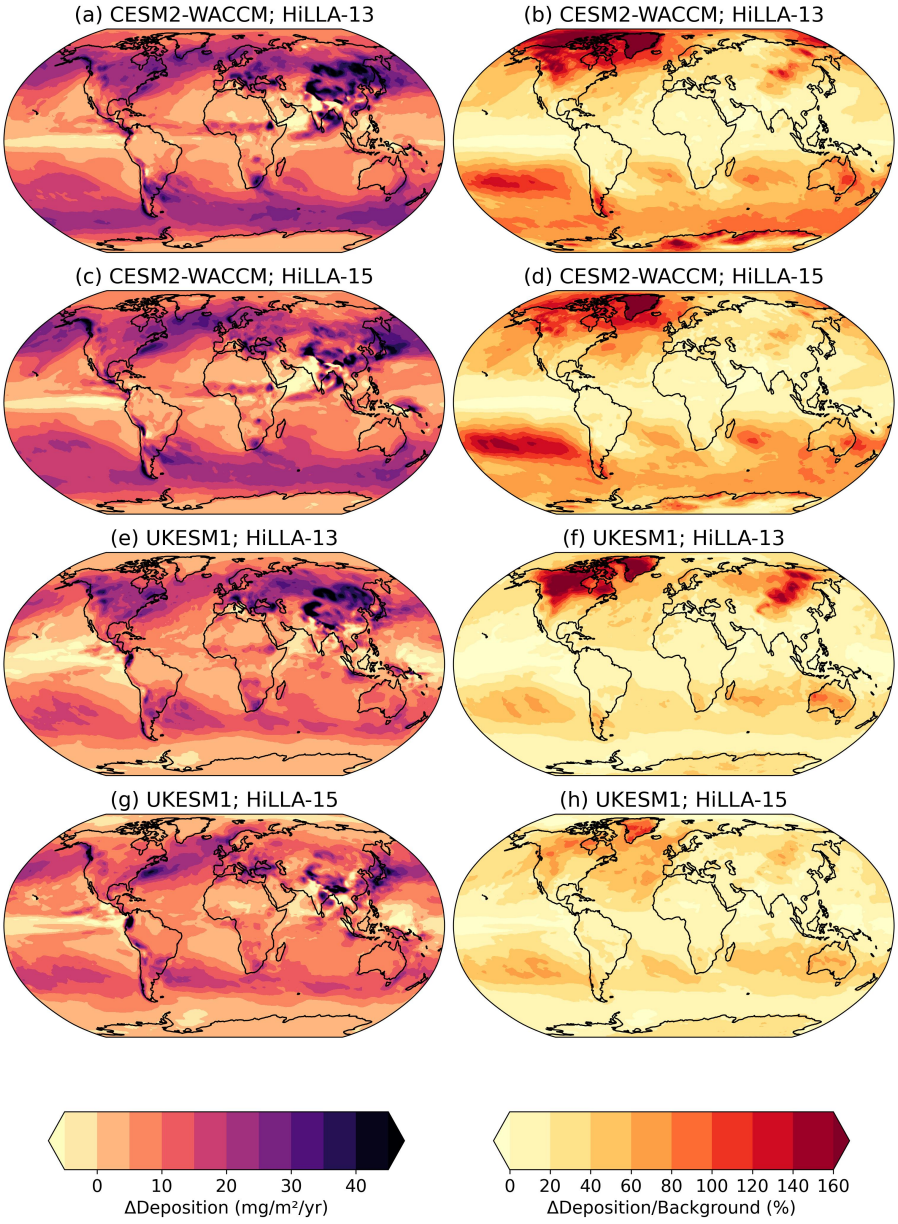

Figure A12. Deposition of SO_4 under HiLLA-SAI in UKESM1 and CESM2-WACCM , in absolute units (milligrams S per m2 per year (left) and as a percentage of the local background deposition under SSP2-4.5 (right). All values are time means over the 20-year period 2050-2069.

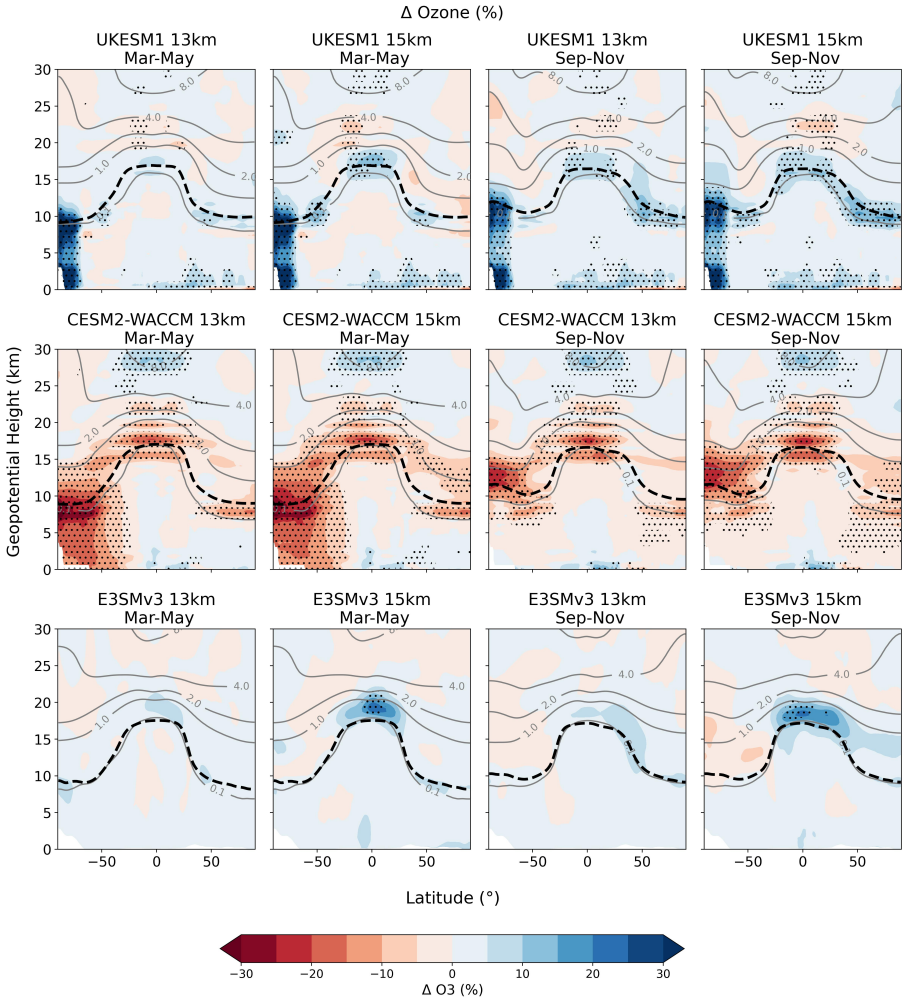

Figure A13. Ozone response - percentage change in ozone concentration relative to the SSP2-4.5 background over the final 20-years of simulations (2050-2069). The gray contours show the background concentration in parts per million. The stippling marks changes which are significant at a 5% False Discovery Rate, following Wilks (2016), using three ensemble members from the SSP2-4.5 scenario for UKESM1 and CESM2-WACCM, but only the single available member for E3SMv3, meaning a larger signal is required for significance in this case. Only CESM2-WACCM has stratospheric heterogeneous chemistry active. The tropopause height in each model is shown as the black dashed line.

Author contributions. AD ran the UKESM1 simulations, performed the analysis and prepared the original manuscript. WL ran the CESM2-WACCM simulations. LW ran the E3SMv3 simulations, with assistance from BW. PI and MT supervised the project. DGM contributed to conceptualization and methodology, along with MH, DV and PI. All authors contributed to review and editing of the manuscript.

Competing interests. The authors declare that no competing interests are present.

Acknowledgements. AD's contribution was funded by the Natural Environment Research Council (NERC) London Doctoral Training Partnership (DTP) Grant NE/S007229/1.

This work was partly supported by the Laboratory Directed Research and Development program at Sandia National Laboratories. Sandia National Laboratories is a multi-mission laboratory managed and operated by National Technology & Engineering Solutions of Sandia, LLC (NTESS), a wholly owned subsidiary of Honeywell International Inc., for the U.S. Department of Energy's National Nuclear Security Administration (DOE/NNSA) under contract DE-NA0003525. This written work is coauthored by an employee of NTESS. The employee, not NTESS, owns the right, title and interest in and to the written work and is responsible for its contents. Any subjective views or opinions that might be expressed in the written work do not necessarily represent the views of the U.S. Government. The publisher acknowledges that the U.S. Government retains a non-exclusive, paid-up, irrevocable, world-wide license to publish or reproduce the published form of this written work or allow others to do so, for U.S. Government purposes. The DOE will provide public access to results of federally sponsored research in accordance with the DOE Public Access Plan. MH is funded by SilverLining through the Safe Climate Research Initiative.

The CESM project is supported primarily by the National Science Foundation. Computational support and computer and data storage services, including the Derecho supercomputer (doi: 10.5065/qx9a-pg09), were provided by the Computational and Information Systems Laboratory (CISL) at NSF NCAR.

Support for WRL has been provided in part by the Quadrature Climate Foundation, Grant No. 01-21-000349.

Support for DGM and DV was provided in part by the Quadrature Climate Foundation.

References

Archibald, A. T., O'Connor, F. M., Abraham, N. L., Archer-Nicholls, S., Chipperfield, M. P., Dalvi, M., Folberth, G. A., Dennison, F., Dhomse, S. S., Griffiths, P. T., Hardacre, C., Hewitt, A. J., Hill, R. S., Johnson, C. E., Keeble, J., Köhler, M. O., Morgenstern, O., Mulcahy, J. P., Ordóñez, C., Pope, R. J., Rumbold, S. T., Russo, M. R., Savage, N. H., Sellar, A., Stringer, M., Turnock, S. T., Wild, O., and Zeng, G.: Description and evaluation of the UKCA stratosphere–troposphere chemistry scheme (StratTrop vn 1.0) implemented in UKESM1, Geoscientific Model Development, 13, 1223–1266, https://doi.org/10.5194/gmd-13-1223-2020, publisher: Copernicus GmbH, 2020.

Armstrong McKay, D. I., Staal, A., Abrams, J. F., Winkelmann, R., Sakschewski, B., Loriani, S., Fetzer, I., Cornell, S. E., Rockström, J., and Lenton, T. M.: Exceeding 1.5°C global warming could trigger multiple climate tipping points, Science, 377, eabn7950, https://doi.org/10.1126/science.abn7950, publisher: American Association for the Advancement of Science, 2022.

Bednarz, E. M., Butler, A. H., Visioni, D., Zhang, Y., Kravitz, B., and MacMartin, D. G.: Injection strategy – a driver of atmospheric circulation and ozone response to stratospheric aerosol geoengineering, Atmospheric Chemistry and Physics, 23, 13 665–13 684, https://doi.org/10.5194/acp-23-13665-2023, publisher: Copernicus GmbH, 2023a.

Bednarz, E. M., Visioni, D., Kravitz, B., Jones, A., Haywood, J. M., Richter, J., MacMartin, D. G., and Braesicke, P.: Climate response to off-equatorial stratospheric sulfur injections in three Earth system models – Part 2: Stratospheric and free-tropospheric response, Atmospheric Chemistry and Physics, 23, 687–709, https://doi.org/10.5194/acp-23-687-2023, publisher: Copernicus GmbH, 2023b.

Berdahl, M., Robock, A., Ji, D., Moore, J. C., Jones, A., Kravitz, B., and Watanabe, S.: Arctic cryosphere response in the Geoengineering Model Intercomparison Project G3 and G4 scenarios, Journal of Geophysical Research: Atmospheres, 119, 1308–1321, https://doi.org/10.1002/2013JD020627, _eprint: https://onlinelibrary.wiley.com/doi/pdf/10.1002/2013JD020627, 2014.

Blanchard-Wrigglesworth, E., Roach, L. A., Donohoe, A., and Ding, Q.: Impact of Winds and Southern Ocean SSTs on Antarctic Sea Ice Trends and Variability, https://doi.org/10.1175/JCLI-D-20-0386.1, section: Journal of Climate, 2021.

Bonan, D. B., Schneider, T., Eisenman, I., and Wills, R. C. J.: Constraining the Date of a Seasonally Ice-Free Arctic Using a Simple Model, Geophysical Research Letters, 48, e2021GL094 309, https://doi.org/10.1029/2021GL094309, _eprint: https://agupubs.onlinelibrary.wiley.com/doi/pdf/10.1029/2021GL094309, 2021.

Bracegirdle, T. J., Krinner, G., Tonelli, M., Haumann, F. A., Naughten, K. A., Rackow, T., Roach, L. A., and Wainer, I.: Twenty first century changes in Antarctic and Southern Ocean surface climate in CMIP6, Atmospheric Science Letters, 21, e984, https://doi.org/10.1002/asl.984, _eprint: https://rmets.onlinelibrary.wiley.com/doi/pdf/10.1002/asl.984, 2020.

Brown, H. Y., Wagman, B., Bull, D., Peterson, K., Hillman, B., Liu, X., Ke, Z., and Lin, L.: Validating a microphysical prognostic stratospheric aerosol implementation in E3SMv2 using observations after the Mount Pinatubo eruption, Geoscientific Model Development, 17, 5087–5121, https://doi.org/10.5194/gmd-17-5087-2024, publisher: Copernicus GmbH, 2024.

Crutzen, P. J.: Albedo Enhancement by Stratospheric Sulfur Injections: A Contribution to Resolve a Policy Dilemma?, Climatic Change, 77, 211, https://doi.org/10.1007/s10584-006-9101-y, 2006.

Danabasoglu, G., Bates, S. C., Briegleb, B. P., Jayne, S. R., Jochum, M., Large, W. G., Peacock, S., and Yeager, S. G.: The CCSM4 Ocean Component, https://doi.org/10.1175/JCLI-D-11-00091.1, section: Journal of Climate, 2012.

Danabasoglu, G., Lamarque, J.-F., Bacmeister, J., Bailey, D. A., DuVivier, A. K., Edwards, J., Emmons, L. K., Fasullo, J., Garcia, R., Gettelman, A., Hannay, C., Holland, M. M., Large, W. G., Lauritzen, P. H., Lawrence, D. M., Lenaerts, J. T. M., Lindsay, K., Lipscomb, W. H., Mills, M. J., Neale, R., Oleson, K. W., Otto-Bliesner, B., Phillips, A. S., Sacks, W., Tilmes, S., van Kampenhout, L., Vertenstein,

M., Bertini, A., Dennis, J., Deser, C., Fischer, C., Fox-Kemper, B., Kay, J. E., Kinnison, D., Kushner, P. J., Larson, V. E., Long, M. C., Mickelson, S., Moore, J. K., Nienhouse, E., Polvani, L., Rasch, P. J., and Strand, W. G.: The Community Earth System Model Version 2 (CESM2), Journal of Advances in Modeling Earth Systems, 12, e2019MS001 916, https://doi.org/10.1029/2019MS001916, _eprint: https://agupubs.onlinelibrary.wiley.com/doi/pdf/10.1029/2019MS001916, 2020.

Duffey, A.: alistairduffey/HiLLA_MM: v1, https://doi.org/10.5281/zenodo.17472547, 2025.

Duffey, A.: alistairduffey/GeoMIP_G6-1.5K_cloud_data: v1.0, https://doi.org/10.5281/zenodo.18715711, 2026.

Duffey, A., Henry, M., Smith, W., Tsamados, M., and Irvine, P. J.: Low-Altitude High-Latitude Stratospheric Aerosol Injection Is Feasible With Existing Aircraft, Earth's Future, 13, e2024EF005 567, https://doi.org/10.1029/2024EF005567, publisher: John Wiley & Sons, Ltd, 2025a.

Duffey, A., Mallett, R., Dutch, V. R., Steckling, J., Hermant, A., Day, J., and Pithan, F.: Representation of Arctic Winter Atmospheric Boundary Layer Stability Over Sea Ice in CMIP6 Models, Journal of Geophysical Research: Atmospheres, 130, e2024JD041 412, https://doi.org/10.1029/2024JD041412, _eprint: https://onlinelibrary.wiley.com/doi/pdf/10.1029/2024JD041412, 2025b.

Duffey, A., Wheeler, L., and Lee, W.: HiLLA-SAI simulations in UKESM1, CESM2-WACCM and E3SMv3, https://doi.org/10.5281/zenodo.17466720, 2025c.

Dykema, J. A., Keith, D. W., and Keutsch, F. N.: Improved aerosol radiative properties as a foundation for solar geoengineering risk assessment, Geophysical Research Letters, 43, 7758–7766, https://doi.org/10.1002/2016GL069258, _eprint: https://onlinelibrary.wiley.com/doi/pdf/10.1002/2016GL069258, 2016.

Eyring, V., Bony, S., Meehl, G. A., Senior, C. A., Stevens, B., Stouffer, R. J., and Taylor, K. E.: Overview of the Coupled Model Intercomparison Project Phase 6 (CMIP6) experimental design and organization, Geoscientific Model Development, 9, 1937–1958, https://doi.org/10.5194/gmd-9-1937-2016, publisher: Copernicus GmbH, 2016.

Fetterer, F., Knowles, K., Meier, W. N., Savoie, M., Windnagel, A., and Stafford, T.: Sea Ice Index, Version 4, https://doi.org/10.7265/A98X-0F50, 2025.

Futerman, G., Adhikari, M., Duffey, A., Fan, Y., Gurevitch, J., Irvine, P., and Wieners, C.: The interaction of solar radiation modification with Earth system tipping elements, Earth System Dynamics, 16, 939–978, https://doi.org/10.5194/esd-16-939-2025, publisher: Copernicus GmbH, 2025.

Gettelman, A., Mills, M. J., Kinnison, D. E., Garcia, R. R., Smith, A. K., Marsh, D. R., Tilmes, S., Vitt, F., Bardeen, C. G., McInerny, J., Liu, H.-L., Solomon, S. C., Polvani, L. M., Emmons, L. K., Lamarque, J.-F., Richter, J. H., Glanville, A. S., Bacmeister, J. T., Phillips, A. S., Neale, R. B., Simpson, I. R., DuVivier, A. K., Hodzic, A., and Randel, W. J.: The Whole Atmosphere Community Climate Model Version 6 (WACCM6), Journal of Geophysical Research: Atmospheres, 124, 12 380–12 403, https://doi.org/10.1029/2019JD030943, _eprint: https://agupubs.onlinelibrary.wiley.com/doi/pdf/10.1029/2019JD030943, 2019.

Goddard, P. B., Kravitz, B., MacMartin, D. G., Visioni, D., Bednarz, E. M., and Lee, W. R.: Stratospheric Aerosol Injection Can Reduce Risks to Antarctic Ice Loss Depending on Injection Location and Amount, Journal of Geophysical Research: Atmospheres, 128, e2023JD039 434, https://doi.org/10.1029/2023JD039434, _eprint: https://agupubs.onlinelibrary.wiley.com/doi/pdf/10.1029/2023JD039434, 2023.

Golaz, J.-C., Van Roekel, L. P., Zheng, X., Roberts, A. F., Wolfe, J. D., Lin, W., Bradley, A. M., Tang, Q., Maltrud, M. E., Forsyth, R. M., Zhang, C., Zhou, T., Zhang, K., Zender, C. S., Wu, M., Wang, H., Turner, A. K., Singh, B., Richter, J. H., Qin, Y., Petersen, M. R., Mametjanov, A., Ma, P.-L., Larson, V. E., Krishna, J., Keen, N. D., Jeffery, N., Hunke, E. C., Hannah, W. M., Guba, O., Griffin, B. M., Feng, Y., Engwirda, D., Di Vittorio, A. V., Dang, C., Conlon, L. M., Chen, C.-C.-J., Brunke, M. A., Bisht, G., Benedict,

J. J., Asay-Davis, X. S., Zhang, Y., Zhang, M., Zeng, X., Xie, S., Wolfram, P. J., Vo, T., Veneziani, M., Tesfa, T. K., Sreepathi, S., Salinger, A. G., Reeves Eyre, J. E. J., Prather, M. J., Mahajan, S., Li, Q., Jones, P. W., Jacob, R. L., Huebler, G. W., Huang, X., Hillman, B. R., Harrop, B. E., Foucar, J. G., Fang, Y., Comeau, D. S., Caldwell, P. M., Bartoletti, T., Balaguru, K., Taylor, M. A., McCoy, R. B., Leung, L. R., and Bader, D. C.: The DOE E3SM Model Version 2: Overview of the Physical Model and Initial Model Evaluation, Journal of Advances in Modeling Earth Systems, 14, e2022MS003 156, https://doi.org/10.1029/2022MS003156, _eprint: https://agupubs.onlinelibrary.wiley.com/doi/pdf/10.1029/2022MS003156, 2022.

Golaz, J.-C., Lin, W., Zheng, X., Xie, S., Roberts, A., Roekel, L. P. V., Thornton, P. E., Barthel, A., Bradley, A., Wolfe, J. D., Zhang, C., Zhang, K., Zhang, S., Asay-Davis, X. S., Begeman, C. B., Bisht, G., Burrows, S. M., Chen, C.-C., Feng, Y., Hunke, E. C., Jacob, R. L., Ke, Z., Mahajan, S., Mahfouz, N., Maltrud, M. E., Shi, X., Tang, Q., Terai, C. R., Thomas, E. E., Wang, H., Xie, J., Zhou, T., Bartoletti, T., Benedict, J. J., Brunke, M., Comeau, D., Fan, J., Forsyth, R. M., Foucar, J. G., Guba, O., Hannah, W. M., Hao, D., Huang, X., Jeffery, N., Kang, H.-G., Keen, N. D., Lee, H.-H., Lee, J., Liu, X., Mametjanov, A., Mülmenstädt, J., Petersen, M. R., Prather, M. J., Price, S., Qian, Y., Salinger, A. G., Santos, S. P., Shan, Y., Singh, B., Smith, K., Song, X., Sreepathi, S., Turner, A. K., Vo, T., Wan, H., Wu, M., Yu, W., Zender, C. S., Zeng, X., Zhang, G. J., Zhang, M., Zhang, T., Yuying, Z., McCoy, R., Taylor, M. A., Leung, L. R., Caldwell, P. M., and Bader, D. C.: The Energy Exascale Earth System Model version 3. Part II: Overview of the coupled system, https://doi.org/10.22541/essoar.175097464.44666291/v1, 2025.

Hahn, L. C., Armour, K. C., Zelinka, M. D., Bitz, C. M., and Donohoe, A.: Contributions to Polar Amplification in CMIP5 and CMIP6 Models, Frontiers in Earth Science, 9, https://www.frontiersin.org/article/10.3389/feart.2021.710036, 2021.

Hausfather, Z.: An assessment of current policy scenarios over the 21st century and the reduced plausibility of high-emissions pathways, Dialogues on Climate Change, 2, 26–32, https://doi.org/10.1177/29768659241304854, publisher: SAGE Publications, 2025.

Haywood, J. M., Jones, A., Bellouin, N., and Stephenson, D.: Asymmetric forcing from stratospheric aerosols impacts Sahelian rainfall, Nature Climate Change, 3, 660–665, https://doi.org/10.1038/nclimate1857, publisher: Nature Publishing Group, 2013.

Henry, M., Haywood, J., Jones, A., Dalvi, M., Wells, A., Visioni, D., Bednarz, E. M., MacMartin, D. G., Lee, W., and Tye, M. R.: Comparison of UKESM1 and CESM2 simulations using the same multi-target stratospheric aerosol injection strategy, Atmospheric Chemistry and Physics, 23, 13 369–13 385, https://doi.org/10.5194/acp-23-13369-2023, publisher: Copernicus GmbH, 2023.

Henry, M., Bednarz, E. M., and Haywood, J.: How does the latitude of stratospheric aerosol injection affect the climate in UKESM1?, Atmospheric Chemistry and Physics, 24, 13 253–13 268, https://doi.org/10.5194/acp-24-13253-2024, publisher: Copernicus GmbH, 2024.

Hersbach, H., Bell, B., Berrisford, P., Hirahara, S., Horányi, A., Muñoz-Sabater, J., Nicolas, J., Peubey, C., Radu, R., Schepers, D., Simmons, A., Soci, C., Abdalla, S., Abellan, X., Balsamo, G., Bechtold, P., Biavati, G., Bidlot, J., Bonavita, M., De Chiara, G., Dahlgren, P., Dee, D., Diamantakis, M., Dragani, R., Flemming, J., Forbes, R., Fuentes, M., Geer, A., Haimberger, L., Healy, S., Hogan, R. J., Hólm, E., Janisková, M., Keeley, S., Laloyaux, P., Lopez, P., Lupu, C., Radnoti, G., de Rosnay, P., Rozum, I., Vamborg, F., Villaume, S., and Thépaut, J.-N.: The ERA5 global reanalysis, Quarterly Journal of the Royal Meteorological Society, 146, 1999–2049, https://doi.org/10.1002/qj.3803, _eprint: https://onlinelibrary.wiley.com/doi/pdf/10.1002/qj.3803, 2020.

Hoffmann, L. and Spang, R.: An assessment of tropopause characteristics of the ERA5 and ERA-Interim meteorological reanalyses, Atmospheric Chemistry and Physics, 22, 4019–4046, https://doi.org/10.5194/acp-22-4019-2022, publisher: Copernicus GmbH, 2022.

Hu, A., Ke, Z., Liu, X., Wagman, B., Brown, H., Lu, Z., Wu, M., Wang, H., Tang, Q., Bull, D., Peterson, K., and Xie, S.: Size-resolved process understanding of stratospheric sulfate aerosol following the Pinatubo eruption, Atmospheric Chemistry and Physics, 25, 12 137–12 157, https://doi.org/10.5194/acp-25-12137-2025, publisher: Copernicus GmbH, 2025.

Intrieri, J. M., Shupe, M. D., Uttal, T., and McCarty, B. J.: An annual cycle of Arctic cloud characteristics observed by radar and lidar at SHEBA, Journal of Geophysical Research: Oceans, 107, SHE 5–1–SHE 5–15, https://doi.org/10.1029/2000JC000423, _eprint: https://agupubs.onlinelibrary.wiley.com/doi/pdf/10.1029/2000JC000423, 2002.

Jiang, J., Cao, L., MacMartin, D. G., Simpson, I. R., Kravitz, B., Cheng, W., Visioni, D., Tilmes, S., Richter, J. H., and Mills, M. J.: Stratospheric Sulfate Aerosol Geoengineering Could Alter the High-Latitude Seasonal Cycle, Geophysical Research Letters, 46, 14 153–14 163, https://doi.org/10.1029/2019GL085758, _eprint: https://onlinelibrary.wiley.com/doi/pdf/10.1029/2019GL085758, 2019.

Jones, A.: MOHC UKESM1.0-LL model output prepared for CMIP6 GeoMIP G6sulfur, https://doi.org/10.22033/ESGF/CMIP6.5822, 2019.

Jones, A., Haywood, J. M., Jones, A. C., Tilmes, S., Kravitz, B., and Robock, A.: North Atlantic Oscillation response in GeoMIP experiments G6solar and G6sulfur: why detailed modelling is needed for understanding regional implications of solar radiation management, Atmospheric Chemistry and Physics, 21, 1287–1304, https://doi.org/10.5194/acp-21-1287-2021, publisher: Copernicus GmbH, 2021.

Jones, A. C., Hawcroft, M. K., Haywood, J. M., Jones, A., Guo, X., and Moore, J. C.: Regional Climate Impacts of Stabilizing Global Warming at 1.5 K Using Solar Geoengineering, Earth's Future, 6, 230–251, https://doi.org/10.1002/2017EF000720, _eprint: https://onlinelibrary.wiley.com/doi/pdf/10.1002/2017EF000720, 2018.

Kleinschmitt, C., Boucher, O., and Platt, U.: Sensitivity of the radiative forcing by stratospheric sulfur geoengineering to the amount and strategy of the SO2 injection studied with the LMDZ-S3A model, Atmospheric Chemistry and Physics, 18, 2769–2786, https://doi.org/10.5194/acp-18-2769-2018, publisher: Copernicus GmbH, 2018.

Kravitz, B., Caldeira, K., Boucher, O., Robock, A., Rasch, P. J., Alterskjær, K., Karam, D. B., Cole, J. N. S., Curry, C. L., Haywood, J. M., Irvine, P. J., Ji, D., Jones, A., Kristjánsson, J. E., Lunt, D. J., Moore, J. C., Niemeier, U., Schmidt, H., Schulz, M., Singh, B., Tilmes, S., Watanabe, S., Yang, S., and Yoon, J.-H.: Climate model response from the Geoengineering Model Intercomparison Project (GeoMIP), Journal of Geophysical Research: Atmospheres, 118, 8320–8332, https://doi.org/10.1002/jgrd.50646, _eprint: https://onlinelibrary.wiley.com/doi/pdf/10.1002/jgrd.50646, 2013.

Kuhlbrodt, T., Jones, C. G., Sellar, A., Storkey, D., Blockley, E., Stringer, M., Hill, R., Graham, T., Ridley, J., Blaker, A., Calvert, D., Copsey, D., Ellis, R., Hewitt, H., Hyder, P., Ineson, S., Mulcahy, J., Siahaan, A., and Walton, J.: The Low-Resolution Version of HadGEM3 GC3.1: Development and Evaluation for Global Climate, Journal of Advances in Modeling Earth Systems, 10, 2865–2888, https://doi.org/10.1029/2018MS001370, _eprint: https://onlinelibrary.wiley.com/doi/pdf/10.1029/2018MS001370, 2018.

Lawrence, D. M., Fisher, R. A., Koven, C. D., Oleson, K. W., Swenson, S. C., Bonan, G., Collier, N., Ghimire, B., van Kampenhout, L., Kennedy, D., Kluzek, E., Lawrence, P. J., Li, F., Li, H., Lombardozzi, D., Riley, W. J., Sacks, W. J., Shi, M., Vertenstein, M., Wieder, W. R., Xu, C., Ali, A. A., Badger, A. M., Bisht, G., van den Broeke, M., Brunke, M. A., Burns, S. P., Buzan, J., Clark, M., Craig, A., Dahlin, K., Drewniak, B., Fisher, J. B., Flanner, M., Fox, A. M., Gentine, P., Hoffman, F., Keppel-Aleks, G., Knox, R., Kumar, S., Lenaerts, J., Leung, L. R., Lipscomb, W. H., Lu, Y., Pandey, A., Pelletier, J. D., Perket, J., Randerson, J. T., Ricciuto, D. M., Sanderson, B. M., Slater, A., Subin, Z. M., Tang, J., Thomas, R. Q., Val Martin, M., and Zeng, X.: The Community Land Model Version 5: Description of New Features, Benchmarking, and Impact of Forcing Uncertainty, Journal of Advances in Modeling Earth Systems, 11, 4245–4287, https://doi.org/10.1029/2018MS001583, _eprint: https://agupubs.onlinelibrary.wiley.com/doi/pdf/10.1029/2018MS001583, 2019.

Lee, W. R., MacMartin, D. G., Visioni, D., and Kravitz, B.: High-Latitude Stratospheric Aerosol Geoengineering Can Be More Effective if Injection Is Limited to Spring, Geophysical Research Letters, 48, e2021GL092 696, https://doi.org/10.1029/2021GL092696, _eprint: https://onlinelibrary.wiley.com/doi/pdf/10.1029/2021GL092696, 2021.

Lee, W. R., MacMartin, D. G., Visioni, D., Kravitz, B., Chen, Y., Moore, J. C., Leguy, G., Lawrence, D. M., and Bailey, D. A.: High-Latitude Stratospheric Aerosol Injection to Preserve the Arctic, Earth's Future, 11, e2022EF003 052, https://doi.org/10.1029/2022EF003052, _eprint: https://onlinelibrary.wiley.com/doi/pdf/10.1029/2022EF003052, 2023a.

Lee, W. R., Visioni, D., Bednarz, E. M., MacMartin, D. G., Kravitz, B., and Tilmes, S.: Quantifying the Efficiency of Stratospheric Aerosol Geoengineering at Different Altitudes, Geophysical Research Letters, 50, e2023GL104 417, https://doi.org/10.1029/2023GL104417, _eprint: https://onlinelibrary.wiley.com/doi/pdf/10.1029/2023GL104417, 2023b.

Lee, W. R., Visioni, D., Wagman, B. M., Wentland, C. R., Kravitz, B., Watanabe, S., Sekiya, T., Jones, A., Haywood, J., Henry, M., and Bednarz, E. M.: G6-1.5K-SAI and G6sulfur: changes in impacts and uncertainty depending on stratospheric aerosol injection strategy in the Geoengineering Model Intercomparison Project, EGUsphere, pp. 1–33, https://doi.org/10.5194/egusphere-2025-5742, publisher: Copernicus GmbH, 2025.

Liu, X., Ma, P.-L., Wang, H., Tilmes, S., Singh, B., Easter, R. C., Ghan, S. J., and Rasch, P. J.: Description and evaluation of a new four-mode version of the Modal Aerosol Module (MAM4) within version 5.3 of the Community Atmosphere Model, Geoscientific Model Development, 9, 505–522, https://doi.org/10.5194/gmd-9-505-2016, publisher: Copernicus GmbH, 2016.

Mann, G. W., Carslaw, K. S., Spracklen, D. V., Ridley, D. A., Manktelow, P. T., Chipperfield, M. P., Pickering, S. J., and Johnson, C. E.: Description and evaluation of GLOMAP-mode: a modal global aerosol microphysics model for the UKCA composition-climate model, Geoscientific Model Development, 3, 519–551, https://doi.org/10.5194/gmd-3-519-2010, publisher: Copernicus GmbH, 2010.

McCrystall, M. R., Stroeve, J., Serreze, M., Forbes, B. C., and Screen, J. A.: New climate models reveal faster and larger increases in Arctic precipitation than previously projected, Nature Communications, 12, 6765, https://doi.org/10.1038/s41467-021-27031-y, number: 1 Publisher: Nature Publishing Group, 2021.

McCusker, K. E., Battisti, D. S., and Bitz, C. M.: Inability of stratospheric sulfate aerosol injections to preserve the West Antarctic Ice Sheet, Geophysical Research Letters, 42, 4989–4997, https://doi.org/10.1002/2015GL064314, _eprint: https://onlinelibrary.wiley.com/doi/pdf/10.1002/2015GL064314, 2015.

Mulcahy, J. P., Jones, C., Sellar, A., Johnson, B., Boutle, I. A., Jones, A., Andrews, T., Rumbold, S. T., Mollard, J., Bellouin, N., Johnson, C. E., Williams, K. D., Grosvenor, D. P., and McCoy, D. T.: Improved Aerosol Processes and Effective Radiative Forcing in HadGEM3 and UKESM1, Journal of Advances in Modeling Earth Systems, 10, 2786–2805, https://doi.org/10.1029/2018MS001464, _eprint: https://onlinelibrary.wiley.com/doi/pdf/10.1029/2018MS001464, 2018.

Mulcahy, J. P., Johnson, C., Jones, C. G., Povey, A. C., Scott, C. E., Sellar, A., Turnock, S. T., Woodhouse, M. T., Abraham, N. L., Andrews, M. B., Bellouin, N., Browse, J., Carslaw, K. S., Dalvi, M., Folberth, G. A., Glover, M., Grosvenor, D. P., Hardacre, C., Hill, R., Johnson, B., Jones, A., Kipling, Z., Mann, G., Mollard, J., O'Connor, F. M., Palmiéri, J., Reddington, C., Rumbold, S. T., Richardson, M., Schutgens, N. A. J., Stier, P., Stringer, M., Tang, Y., Walton, J., Woodward, S., and Yool, A.: Description and evaluation of aerosol in UKESM1 and HadGEM3-GC3.1 CMIP6 historical simulations, Geoscientific Model Development, 13, 6383–6423, https://doi.org/10.5194/gmd-13-6383-2020, publisher: Copernicus GmbH, 2020.

NASEM: Reflecting Sunlight: Recommendations for Solar Geoengineering Research and Research Governance, The National Academies Press, Washington, DC, ISBN 978-0-309-67605-2, https://doi.org/10.17226/25762, 2021.

Niemeier, U., Schmidt, H., and Timmreck, C.: The dependency of geoengineered sulfate aerosol on the emission strategy, Atmospheric Science Letters, 12, 189–194, https://doi.org/10.1002/asl.304, _eprint: https://onlinelibrary.wiley.com/doi/pdf/10.1002/asl.304, 2011.

North, G. R., Cahalan, R. F., and Coakley Jr., J. A.: Energy balance climate models, Reviews of Geophysics, 19, 91–121, https://doi.org/10.1029/RG019i001p00091, _eprint: https://agupubs.onlinelibrary.wiley.com/doi/pdf/10.1029/RG019i001p00091, 1981.

Notz, D. and Community, S.: Arctic Sea Ice in CMIP6, Geophysical Research Letters, 47, e2019GL086 749, https://doi.org/10.1029/2019GL086749, _eprint: https://onlinelibrary.wiley.com/doi/pdf/10.1029/2019GL086749, 2020.

Notz, D. and Stroeve, J.: The Trajectory Towards a Seasonally Ice-Free Arctic Ocean, Current Climate Change Reports, 4, 407–416, https://doi.org/10.1007/s40641-018-0113-2, 2018.

O'Neill, B. C., Tebaldi, C., van Vuuren, D. P., Eyring, V., Friedlingstein, P., Hurtt, G., Knutti, R., Kriegler, E., Lamarque, J.-F., Lowe, J., Meehl, G. A., Moss, R., Riahi, K., and Sanderson, B. M.: The Scenario Model Intercomparison Project (ScenarioMIP) for CMIP6, Geoscientific Model Development, 9, 3461–3482, https://doi.org/10.5194/gmd-9-3461-2016, publisher: Copernicus GmbH, 2016.

Pithan, F. and Mauritsen, T.: Arctic amplification dominated by temperature feedbacks in contemporary climate models, Nature Geoscience, 7, 181–184, https://doi.org/10.1038/ngeo2071, number: 3 Publisher: Nature Publishing Group, 2014.

Rantanen, M., Karpechko, A. Y., Lipponen, A., Nordling, K., Hyvärinen, O., Ruosteenoja, K., Vihma, T., and Laaksonen, A.: The Arctic has warmed nearly four times faster than the globe since 1979, Communications Earth & Environment, 3, 1–10, https://doi.org/10.1038/s43247-022-00498-3, number: 1 Publisher: Nature Publishing Group, 2022.

Richter, J. H., Visioni, D., MacMartin, D. G., Bailey, D. A., Rosenbloom, N., Dobbins, B., Lee, W. R., Tye, M., and Lamarque, J.-F.: Assessing Responses and Impacts of Solar climate intervention on the Earth system with stratospheric aerosol injection (ARISE-SAI): protocol and initial results from the first simulations, Geoscientific Model Development, 15, 8221–8243, https://doi.org/10.5194/gmd-15-8221-2022, publisher: Copernicus GmbH, 2022.

Ridley, J. K., Lowe, J. A., and Hewitt, H. T.: How reversible is sea ice loss?, The Cryosphere, 6, 193–198, https://doi.org/10.5194/tc-6-193-2012, publisher: Copernicus GmbH, 2012.

Robock, A.: Volcanic eruptions and climate, Reviews of Geophysics, 38, 191–219, https://doi.org/10.1029/1998RG000054, _eprint: https://onlinelibrary.wiley.com/doi/pdf/10.1029/1998RG000054, 2000.

Robock, A.: The Latest on Volcanic Eruptions and Climate, Eos, Transactions American Geophysical Union, 94, 305–306, https://doi.org/10.1002/2013EO350001, _eprint: https://onlinelibrary.wiley.com/doi/pdf/10.1002/2013EO350001, 2013.

Robock, A. and Mao, J.: Winter warming from large volcanic eruptions, Geophysical Research Letters, 19, 2405–2408, https://doi.org/10.1029/92GL02627, _eprint: https://agupubs.onlinelibrary.wiley.com/doi/pdf/10.1029/92GL02627, 1992.

Robock, A., Oman, L., and Stenchikov, G. L.: Regional climate responses to geoengineering with tropical and Arctic SO2 injections, Journal of Geophysical Research: Atmospheres, 113, https://doi.org/10.1029/2008JD010050, _eprint: https://onlinelibrary.wiley.com/doi/pdf/10.1029/2008JD010050, 2008.

Schneider, D. P., Ammann, C. M., Otto-Bliesner, B. L., and Kaufman, D. S.: Climate response to large, high-latitude and low-latitude volcanic eruptions in the Community Climate System Model, Journal of Geophysical Research: Atmospheres, 114, https://doi.org/10.1029/2008JD011222, _eprint: https://agupubs.onlinelibrary.wiley.com/doi/pdf/10.1029/2008JD011222, 2009.

Sellar, A. A., Jones, C. G., Mulcahy, J. P., Tang, Y., Yool, A., Wiltshire, A., O'Connor, F. M., Stringer, M., Hill, R., Palmieri, J., Woodward, S., de Mora, L., Kuhlbrodt, T., Rumbold, S. T., Kelley, D. I., Ellis, R., Johnson, C. E., Walton, J., Abraham, N. L., Andrews, M. B., Andrews, T., Archibald, A. T., Berthou, S., Burke, E., Blockley, E., Carslaw, K., Dalvi, M., Edwards, J., Folberth, G. A., Gedney, N., Griffiths, P. T., Harper, A. B., Hendry, M. A., Hewitt, A. J., Johnson, B., Jones, A., Jones, C. D., Keeble, J., Liddicoat, S., Morgenstern, O., Parker, R. J., Predoi, V., Robertson, E., Siahaan, A., Smith, R. S., Swaminathan, R., Woodhouse, M. T., Zeng, G., and Zerroukat, M.: UKESM1: Description and Evaluation of the U.K. Earth System Model, Journal of Advances in Modeling Earth Systems, 11, 4513–4558, https://doi.org/10.1029/2019MS001739, _eprint: https://onlinelibrary.wiley.com/doi/pdf/10.1029/2019MS001739, 2019.

Serreze, M. C. and Francis, J. A.: The Arctic Amplification Debate, Climatic Change, 76, 241–264, https://doi.org/10.1007/s10584-005-9017-y, 2006.

Sjolte, J., Adolphi, F., Guðlaugsdòttir, H., and Muscheler, R.: Major Differences in Regional Climate Impact Between High- and Low-Latitude Volcanic Eruptions, Geophysical Research Letters, 48, e2020GL092 017, https://doi.org/10.1029/2020GL092017, _eprint: https://agupubs.onlinelibrary.wiley.com/doi/pdf/10.1029/2020GL092017, 2021.

Smith, K. M., Barthel, A. M., Conlon, L. M., Van Roekel, L. P., Bartoletti, A., Golaz, J.-C., Zhang, C., Begeman, C. B., Benedict, J. J., Bisht, G., Feng, Y., Hannah, W., Harrop, B. E., Jeffery, N., Lin, W., Ma, P.-L., Maltrud, M. E., Petersen, M. R., Singh, B., Tang, Q., Tesfa, T., Wolfe, J. D., Xie, S., Zheng, X., Balaguru, K., Garuba, O., Gleckler, P., Hu, A., Lee, J., Moore-Maley, B., and Ordoñez, A. C.: The DOE E3SM version 2.1: overview and assessment of the impacts of parameterized ocean submesoscales, Geoscientific Model Development, 18, 1613–1633, https://doi.org/10.5194/gmd-18-1613-2025, publisher: Copernicus GmbH, 2025.

Smith, R., Jones, P., Briegleb, B., Bryan, F., Danabasoglu, G., Dennis, J., Dukowicz, J., Eden, C., Fox-Kemper, B., Gent, P., Hecht, M., Jayne, S., Jochum, M., Large, W., Lindsay, K., Maltrud, M., Norton, N., Peacock, S., Vertenstein, M., and Yeager, S.: The Parallel Ocean Program (POP) Reference Manual, 2010.

Smith, W.: An assessment of the infrastructural and temporal barriers constraining a near-term implementation of a global stratospheric aerosol injection program, Environmental Research Communications, 6, 061 007, https://doi.org/10.1088/2515-7620/ad4f5c, publisher: IOP Publishing, 2024.

Smith, W., Bartels, M. F., Boers, J. G., and Rice, C. V.: On Thin Ice: Solar Geoengineering to Manage Tipping Element Risks in the Cryosphere by 2040, Earth's Future, 12, e2024EF004 797, https://doi.org/10.1029/2024EF004797, _eprint: https://onlinelibrary.wiley.com/doi/pdf/10.1029/2024EF004797, 2024.

Stenchikov, G., Robock, A., Ramaswamy, V., Schwarzkopf, M. D., Hamilton, K., and Ramachandran, S.: Arctic Oscillation response to the 1991 Mount Pinatubo eruption: Effects of volcanic aerosols and ozone depletion, Journal of Geophysical Research: Atmospheres, 107, ACL 28–1–ACL 28–16, https://doi.org/10.1029/2002JD002090, _eprint: https://agupubs.onlinelibrary.wiley.com/doi/pdf/10.1029/2002JD002090, 2002.

Taylor, P. C., Boeke, R. C., Boisvert, L. N., Feldl, N., Henry, M., Huang, Y., Langen, P. L., Liu, W., Pithan, F., Sejas, S. A., and Tan, I.: Process Drivers, Inter-Model Spread, and the Path Forward: A Review of Amplified Arctic Warming, Frontiers in Earth Science, 9, https://www.frontiersin.org/articles/10.3389/feart.2021.758361, 2022.

Tilmes, S., Richter, J. H., Mills, M. J., Kravitz, B., MacMartin, D. G., Vitt, F., Tribbia, J. J., and Lamarque, J.-F.: Sensitivity of Aerosol Distribution and Climate Response to Stratospheric SO2 Injection Locations, Journal of Geophysical Research: Atmospheres, 122, 12,591–12,615, https://doi.org/10.1002/2017JD026888, _eprint: https://onlinelibrary.wiley.com/doi/pdf/10.1002/2017JD026888, 2017.

Tilmes, S., Richter, J. H., Mills, M. J., Kravitz, B., MacMartin, D. G., Garcia, R. R., Kinnison, D. E., Lamarque, J.-F., Tribbia, J., and Vitt, F.: Effects of Different Stratospheric SO2 Injection Altitudes on Stratospheric Chemistry and Dynamics, Journal of Geophysical Research: Atmospheres, 123, 4654–4673, https://doi.org/10.1002/2017JD028146, _eprint: https://agupubs.onlinelibrary.wiley.com/doi/pdf/10.1002/2017JD028146, 2018.

Tilmes, S., MacMartin, D. G., Lenaerts, J. T. M., van Kampenhout, L., Muntjewerf, L., Xia, L., Harrison, C. S., Krumhardt, K. M., Mills, M. J., Kravitz, B., and Robock, A.: Reaching 1.5 and 2.0 °C global surface temperature targets using stratospheric aerosol geoengineering, Earth System Dynamics, 11, 579–601, https://doi.org/10.5194/esd-11-579-2020, publisher: Copernicus GmbH, 2020.

Tilmes, S., Richter, J. H., Kravitz, B., MacMartin, D. G., Glanville, A. S., Visioni, D., Kinnison, D. E., and Müller, R.: Sensitivity of Total Column Ozone to Stratospheric Sulfur Injection Strategies, Geophysical Research Letters, 48, e2021GL094 058, https://doi.org/10.1029/2021GL094058, _eprint: https://agupubs.onlinelibrary.wiley.com/doi/pdf/10.1029/2021GL094058, 2021.

UNEP: One Atmosphere: An Independent Expert Review on Solar Radiation Modification Research and Deployment, https://wedocs.unep.org/20.500.11822/41903, 2023.

Visioni, D., Slessarev, E., MacMartin, D. G., Mahowald, N. M., Goodale, C. L., and Xia, L.: What goes up must come down: impacts of deposition in a sulfate geoengineering scenario, Environmental Research Letters, 15, 094 063, https://doi.org/10.1088/1748-9326/ab94eb, publisher: IOP Publishing, 2020.

Visioni, D., Bednarz, E. M., Lee, W. R., Kravitz, B., Jones, A., Haywood, J. M., and MacMartin, D. G.: Climate response to off-equatorial stratospheric sulfur injections in three Earth system models – Part 1: Experimental protocols and surface changes, Atmospheric Chemistry and Physics, 23, 663–685, https://doi.org/10.5194/acp-23-663-2023, publisher: Copernicus GmbH, 2023.

Visioni, D., Robock, A., Haywood, J., Henry, M., Tilmes, S., MacMartin, D. G., Kravitz, B., Doherty, S. J., Moore, J., Lennard, C., Watanabe, S., Muri, H., Niemeier, U., Boucher, O., Syed, A., Egbebiyi, T. S., Séférian, R., and Quaglia, I.: G6-1.5K-SAI: a new Geoengineering Model Intercomparison Project (GeoMIP) experiment integrating recent advances in solar radiation modification studies, Geoscientific Model Development, 17, 2583–2596, https://doi.org/10.5194/gmd-17-2583-2024, publisher: Copernicus GmbH, 2024.

Visioni, D., Robock, A., Roberts, K. E., Lee, W., Henry, M., Duffey, A., Hirasawa, H., Chegwidden, O., and Sipra, H.: Finalizing experimental protocols for the Geoengineering Model Intercomparison Project (GeoMIP) contribution to CMIP7, https://doi.org/10.1175/BAMS-D-25-0191.1, section: Bulletin of the American Meteorological Society, 2025.

Walters, D., Baran, A. J., Boutle, I., Brooks, M., Earnshaw, P., Edwards, J., Furtado, K., Hill, P., Lock, A., Manners, J., Morcrette, C., Mulcahy, J., Sanchez, C., Smith, C., Stratton, R., Tennant, W., Tomassini, L., Van Weverberg, K., Vosper, S., Willett, M., Browse, J., Bushell, A., Carslaw, K., Dalvi, M., Essery, R., Gedney, N., Hardiman, S., Johnson, B., Johnson, C., Jones, A., Jones, C., Mann, G., Milton, S., Rumbold, H., Sellar, A., Ujiie, M., Whitall, M., Williams, K., and Zerroukat, M.: The Met Office Unified Model Global Atmosphere 7.0/7.1 and JULES Global Land 7.0 configurations, Geoscientific Model Development, 12, 1909–1963, https://doi.org/10.5194/gmd-12-1909-2019, publisher: Copernicus GmbH, 2019.

Wheeler, L., Wagman, B., Smith, W., Davies, P., Cook, B., Brunell, S., Glen, A., Hackenburg, D., Lien, J., Shand, L., and Zeitler, T.: Design and simulation of a logistically constrained high-latitude, low-altitude stratospheric aerosol injection scenario in the Energy Exascale Earth System Model (E3SM), Environmental Research Letters, 20, 044 011, https://doi.org/10.1088/1748-9326/adba01, publisher: IOP Publishing, 2025.

Wilks, D. S.: "The Stippling Shows Statistically Significant Grid Points": How Research Results are Routinely Overstated and Overinterpreted, and What to Do about It, https://doi.org/10.1175/BAMS-D-15-00267.1, section: Bulletin of the American Meteorological Society, 2016.

Xie, S., Terai, C. R., Wang, H., Tang, Q., Fan, J., Burrows, S. M., Lin, W., Wu, M., Song, X., Zhang, Y., Taylor, M. A., Golaz, J.-C., Benedict, J. J., Chen, C.-C., Feng, Y., Hannah, W. M., Ke, Z., Shan, Y., Larson, V. E., Liu, X., Prather, M. J., Richter, J. H., Shrivastava, M., Wan, H., Zhang, G. J., Zhang, K., Bradley, A., Cameron-Smith, P. J., Damiano, L., Debusschere, B., Donahue, A. S., Easter, R. C., Eldred, M. S., Griffin, B. M., Guba, O., Guo, Z., Huang, X., Lee, J., Lee, H.-H., Lou, S., Mahfouz, N., Moncrieff, M. W., Mülmenstädt, J., Qian, Y., Rasool, Q. Z., Roberts, A., Santos, S. P., Sargsyan, K., Shpund, J., Singh, B., Tao, C., Xie, J., Yang, Y., Zeng, X., Zhang, C., Zhang, M., Zhang, S., Zhang, T., Zheng, X., Jacob, R. L., Leung, L. R., McCoy, R., and Bader, D. C.: The Energy Exascale Earth System Model Version 3. Part I: Overview of the Atmospheric Component, https://doi.org/10.22541/essoar.174456922.21825772/v1, 2025.

Zambri, B. and Robock, A.: Winter warming and summer monsoon reduction after volcanic eruptions in Coupled Model Intercomparison Project 5 (CMIP5) simulations, Geophysical Research Letters, 43, 10,920–10,928, https://doi.org/10.1002/2016GL070460, _eprint: https://agupubs.onlinelibrary.wiley.com/doi/pdf/10.1002/2016GL070460, 2016.

Zhang, Y., MacMartin, D. G., Visioni, D., Bednarz, E. M., and Kravitz, B.: Hemispherically symmetric strategies for stratospheric aerosol injection, Earth System Dynamics, 15, 191–213, https://doi.org/10.5194/esd-15-191-2024, publisher: Copernicus GmbH, 2024.